

First Submillimeter Lights from Dome A: Tracing the Carbon Cycle in the Feedback of Massive Stars

Yan Gong^{1†}, Jiaqiang Zhong^{1,3†}, Yuan Ren^{1,3}, Yilong Zhang^{1,3}, Daizhong Liu¹,
 Yiping Ao^{1,3}, Qijun Yao¹, Wen Zhang^{1,3}, Wei Miao^{1,3}, Zhenhui Lin^{1,3},
 Wenying Duan^{1,2}, Dong Liu¹, Kangmin Zhou¹, Jie Liu¹, Zheng Wang¹, Junda Jin¹,
 Kun Zhang¹, Feng Wu¹, Jinpeng Li¹, Boliang Liu¹, Xuan Zhang^{1,3}, Zhengheng Luo^{1,2},
 Jiameng Wang^{1,2}, Huiqian Hao⁴, Xingming Lu⁴, Shaoming Xie⁴, Jia Quan⁵,
 Yanjie Liu⁵, Jingtao Liang⁵, Xianjin Deng^{6,7}, Jun Jiang^{6,7}, Li Li^{6,7},
 Liang Guo⁸, Tuo Ji⁹, Peng Jiang⁹, Yi Zhang¹⁰, Chenggang Shu¹⁰,
 Sudeep Neupane¹¹, Ruiqing Mao¹, Shengcai Shi¹, Jing Li^{1*}

¹ Purple Mountain Observatory and Key Laboratory of Radio Astronomy, Chinese Academy of Sciences,
 Nanjing 210008, China

² School of Astronomy and Space Sciences, University of Science and Technology of China, Hefei 230026, China

³ State Key Laboratory of Radio Astronomy and Technology, National Astronomical Observatories,
 Chinese Academy of Sciences, Beijing 100101, China

⁴ The 54th Research Institute of China Electronics Technology Group Corporation, Shijiazhuang 050081, China

⁵ Technical Institute of Physics and Chemistry, Chinese Academy of Sciences, Beijing 100190, China

⁶ Microsystem and Terahertz Research Center, China Academy of Engineering Physics,
 Chengdu, Sichuan 610200, China

⁷ Institute of Electronic Engineering, China Academy of Engineering Physics, Mianyang, Sichuan 621999, China

⁸ Changchun Institute of Optics, Fine Mechanics and Physics, Chinese Academy of Sciences, Changchun 130033, China

⁹ Polar Research Institute of China; Key Laboratory for Polar Science, MNR, Shanghai 200136, China

¹⁰ Shanghai Key Lab for Astrophysics, Shanghai Normal University, 100 Guilin Road, Shanghai 200234, China

¹¹ Max-Planck-Institut für Radioastronomie, Auf dem Hügel 69, D-53121 Bonn, Germany

*Corresponding author. Email: lijing@pmo.ac.cn

[†]These authors contributed equally to this work.

Teaser: First submillimeter maps from Antarctica's Dome A reveal how massive stars power the cosmic carbon cycle.

The cycling of carbon between its ionized, atomic, and molecular phases shapes the chemical compositions and physical conditions of the interstellar medium (ISM). However, ground-based studies of the full carbon cycle have been limited by atmospheric absorption. Dome A, the most promising site for submillimeter astronomy, has long resisted successful submillimeter astronomical observations. Using the 60 cm Antarctic Terahertz Explorer, we present the first successful CO (4 – 3) and [CI] ($^3P_1 - ^3P_0$) mapping observations of two archetypal triggered massive star-formation regions at Dome A. These data, together with archival [CII], provide the first complete characterization of all three carbon phases in these environments. We find elevated C⁰/CO abundance ratios in high-extinction regions, plausibly driven by deep penetration of intense radiation fields from massive stars into a clumpy ISM. These findings mark a major milestone for submillimeter astronomy at Dome A and offer valuable insights into the impact of massive star feedback on the surrounding ISM.

Introduction

Carbon, the second most abundant metal in the universe after oxygen (1), plays a fundamental role in interstellar chemistry and the emergence of life on Earth (2). In the interstellar medium

(ISM), carbon transitions between three primary phases: ionized (C^+), atomic (C^0), and molecular, predominantly in the form of carbon monoxide (CO). This phase cycling governs the thermal balance, molecular complexity, and star formation processes that drive the chemical evolution of galaxies. Known as the stellar nurseries in the ISM, molecular clouds are typically traced using line emission from low J CO rotational transitions (3, 4, 5), yet a substantial fraction of molecular gas extends beyond CO-bright regions (6, 7). In the outer layers of molecular clouds, carbon predominantly exists as C^0 or C^+ , while molecular hydrogen (H_2) is shielded from UV photodissociation by dust or self-shielding (8). However, CO, more vulnerable to photodissociation, becomes depleted in UV-irradiated regions (9), leading to an H_2 component that is “dark” in CO emission. With an ionization potential of 11.3 eV lower than hydrogen’s ionization potential of 13.6 eV, carbon is readily ionized by UV radiation, allowing C^+ to exist in both ionized and neutral gas. C^0 , located between C^+ and CO in the carbon cycle, is abundant in the intermediate layers of PDRs where UV photons dissociate CO but are insufficient to ionize all carbon atoms. C^+ and C^0 thus offer complementary diagnostics to CO, tracing diffuse and CO-dark molecular gas. Therefore, a comprehensive view of carbon across its ionized, atomic, and molecular phases provides a powerful diagnostic of the composition, structure, and evolution of the ISM.

In classic PDR models (8, 10, 11), CO molecules are photodissociated into atomic carbon (C^0), which can be further ionized to C^+ under strong UV radiation. This suggests that C^0 and C^+ serve as unique tracers of environments inaccessible to CO. The [CII] 158 μ m line, a key tracer of C^+ , has been shown to reveal cloud kinematics that remain undetected in CO observations (12, 13, 14), reinforcing this scenario. However, [CII] 158 μ m emission can arise from molecular, atomic, and ionized gas (15, 16, 17), complicating its interpretation. In contrast, the two fine-structure transitions of C^0 in its ground state, $^3P_1 - ^3P_0$ (492 GHz) and $^3P_2 - ^3P_1$ (809 GHz), are powerful tracers of molecular gas (18, 19, 20, 21), with negligible contributions from atomic or ionized gas. This characteristic highlights the advantage of C^0 transitions in studying PDRs, which are crucial for understanding massive star feedback and cloud formation processes. However, observing [CI] emission remains challenging due to poor atmospheric transmission at these frequencies. While ground-based telescopes have successfully detected [CI] emissions, such observations remain limited compared to the extensive CO surveys. A submillimeter telescope at an exceptional observing site is therefore essential to enable a more comprehensive exploration of the carbon cycle.

on large scales in the ISM. This ambition has already driven the development of next-generation submillimeter observatories (22, 23).

Results and discussion

The Road to First Submillimeter Lights at Dome A

In 2005, the Chinese expedition successfully reached Dome A (24), the summit of the East Antarctic ice sheet, a site considered highly promising for submillimeter observations (25). In 2009, the Chinese Kunlun Station was successfully established at Dome A, providing a permanent research base for year-round scientific operations. Based on a remotely operated Fourier transform spectrometer deployed to Dome A during the 26th Chinese National Antarctica and Arctic Research Expedition (CHINARE), atmospheric radiation measurements across the full water vapor pure rotation band (0.75 THz to 15 THz) reveal substantial transmission within numerous frequency windows, underscoring the emergence of terahertz windows at this high-altitude Antarctic site (26). Satellite data further confirm that Dome A exhibits the lowest median precipitable water vapor with the smallest fluctuation (27). Its excellent weather conditions fueled proposals for large-aperture terahertz telescopes and interferometers at the site (28). However, astronomical observations at Dome A pose significant challenges due to its remote location and harsh environmental conditions, including severe cold, persistent snow cover, and the absence of infrastructure. During the 24th CHINARE, the Pre-HEAT instrument, which is a 20 cm aperture submillimeter-wave telescope equipped with a 660 GHz Schottky diode heterodyne receiver (29), was employed to observe ^{13}CO (6 – 5) for only one season at Dome A (30), but the observational results seem to be not available in the literature, leaving the conclusions elusive. While successful submillimeter observations have been made at other Antarctic locations, submillimeter observations at Dome A have yet to be fully realized.

Due to its challenging environmental conditions, no submillimeter telescopes have been operational at Dome A since the decommissioning of Pre-HEAT in 2008. However, thanks to the efforts of the 39th, 40th, and 41st expeditions of CHINARE, we had the opportunity to deploy portable submillimeter telescopes to this site. In particular, the Antarctic Terahertz Explorer with a

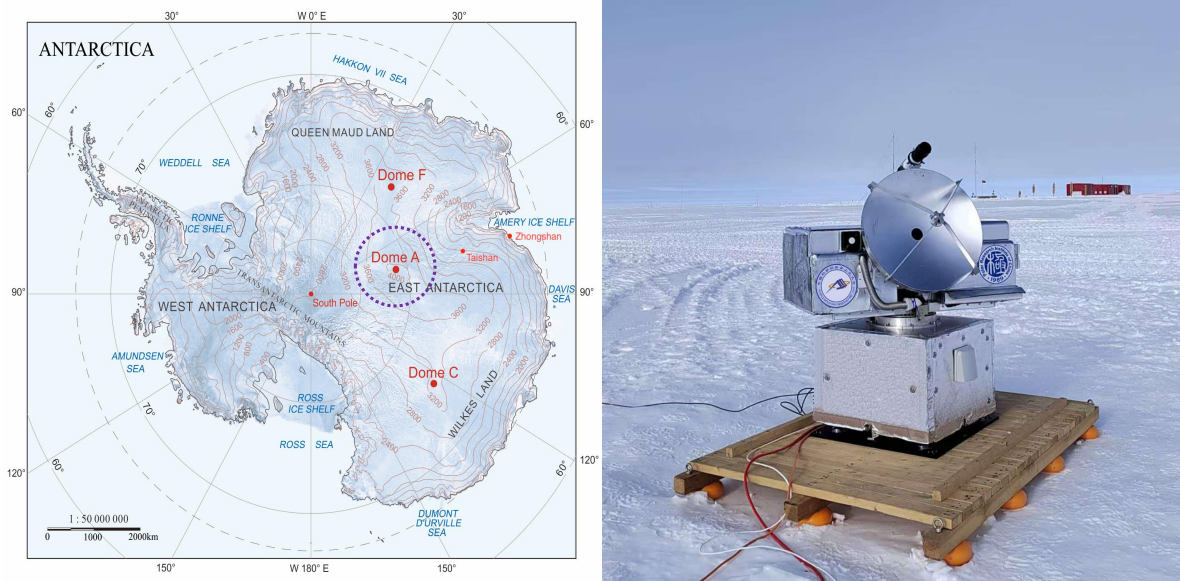


Figure 1: Map of Antarctica with elevation contour lines (30), with Dome A highlighted. Reproduced by permission of RAA. All rights reserved. The right inset shows a photo of ATE60 deployed at Dome A in January 2025 during the 41st CHINARE. The red building discernible in the distant background is the Chinese Kunlun Station.

60 cm aperture (ATE60), a small-size submillimeter telescope equipped with a 460 GHz Nb-based Superconductor-Insulator-Superconductor (SIS) heterodyne receiver specifically designed for operation in polar conditions, was installed and operated at Dome A in January 2025 during the 41st CHINARE (see Figure 1). SIS heterodyne receivers achieve substantially lower receiver temperatures than Schottky diode receivers (31) previously used for Pre-HEAT, providing a markedly improved opportunity for successful submillimeter observations under the extreme conditions at Dome A. Despite the extremely harsh environment, we successfully carried out commissioning ATE60 observations of the CO (4 – 3) and [CI] ($^3P_1 - ^3P_0$) lines toward two archetypal triggered massive star-formation regions (i.e., RCW 79 and RCW 120) which exhibit prominent, well-defined ring-like morphologies in their PDRs (see Figure 2; more details are given in Section *Source Selection* of the supplementary materials). These observations represent a significant milestone for submillimeter astronomy at Dome A, demonstrating the feasibility of high-frequency observations in one of the most challenging environments on Earth.

The Carbon Cycle and Stellar Feedback Revealed by ATE60

The successful observations provide valuable CO (4 – 3) and [CI] ($^3P_1 - ^3P_0$) data for investigating physical conditions of the ISM. Figure 3 presents the CO (4 – 3) and [CI] ($^3P_1 - ^3P_0$) results toward RCW 79 and RCW 120. Despite the existence of low- J CO and [CII] 158 μm observations (32, 33, 13, 34, 35, 36), we present the first CO (4 – 3) and [CI] ($^3P_1 - ^3P_0$) mapping of RCW 79 and RCW 120 (see Section *Materials and Methods* in the supplementary materials for the details). In particular, the atomic carbon phase can be only investigated with [CI] data, while the CO (4 – 3) transition, with its higher upper-state energy and critical density compared to low- J CO lines, offers enhanced sensitivity to warmer and denser gas components. Hence, our ATE60 observations of [CI] emission bridge a crucial gap in the carbon cycle, providing a complete picture of carbon phases in these regions.

In both regions, bright [CI] and CO (4–3) emission is observed at the peripheries of the H II regions, peaking toward sites of second-generation star formation (37, 38, 39). In RCW 79, the peak positions of the [CII], [CI], and CO (4 – 3) emissions are spatially coincident (Figure 3A–3B), indicating a close association of these tracers in this region. In contrast, in RCW 120, both CO

and [CI] emissions are confined to the southeastern part of the more extended [CII] distribution (Figure 3C–3D). These contrasting morphologies highlight the ability of [CII] to trace more diffuse and extended gas than either [CI] or CO. Moreover, [CI] emission shows a spatial distribution that closely follows that of CO, indicating that both trace similar molecular gas components. In particular, the [CI] emission exhibits a closer morphological correspondence with ^{13}CO than with ^{12}CO (Figure 4A–4B), which is likely attributed to the lower optical depths of the ^{13}CO transitions relative to the ^{12}CO transitions. The agreement between the [CI] and CO distributions is consistent with previous observations of the Orion A molecular cloud (40, 41), indicating that C⁰ is not confined to the cloud surface but also traces the inner part of molecular clouds.

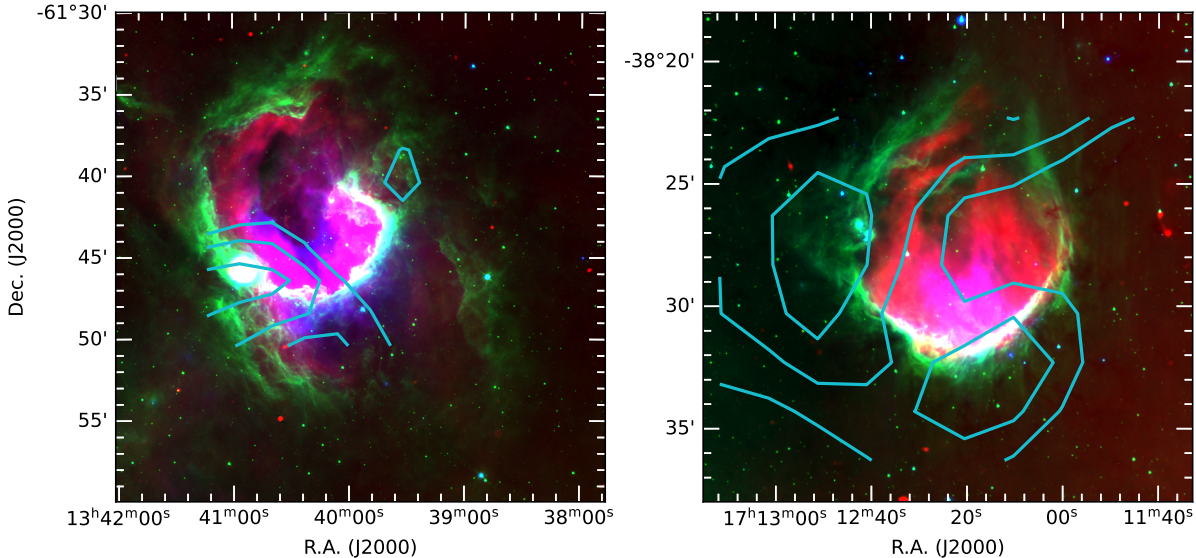


Figure 2: Three-color composite images of RCW 79 (left) and RCW 120 (right) overlaid with ATE60 [CI] integrated intensity contours. The SARAO (South African Radio Astronomy Observatory) MeerKAT Galactic Plane Survey (SMGPS) 1.3 GHz radio continuum emission, Galactic Legacy Infrared Mid-Plane Survey Extraordinaire (GLIMPSE) 8 μm emission, and Multiband Imaging Photometer for Spitzer Galactic Plane Survey (MIPSGAL) 24 μm emission are shown in red, green, and blue, respectively. For RCW 79 and RCW 120, the [CI] integrated intensity maps span velocity ranges of -48 km s^{-1} to -43 km s^{-1} and -13 km s^{-1} to -3 km s^{-1} , respectively. Contours are drawn at 4.5 K km s^{-1} with increments of 1.5 K km s^{-1} for RCW 79, and at 15 K km s^{-1} with increments of 4.5 K km s^{-1} for RCW 120.

Figures 3E and 3F present the average spectra of [CII], [CI], and CO (4 – 3) toward RCW 79

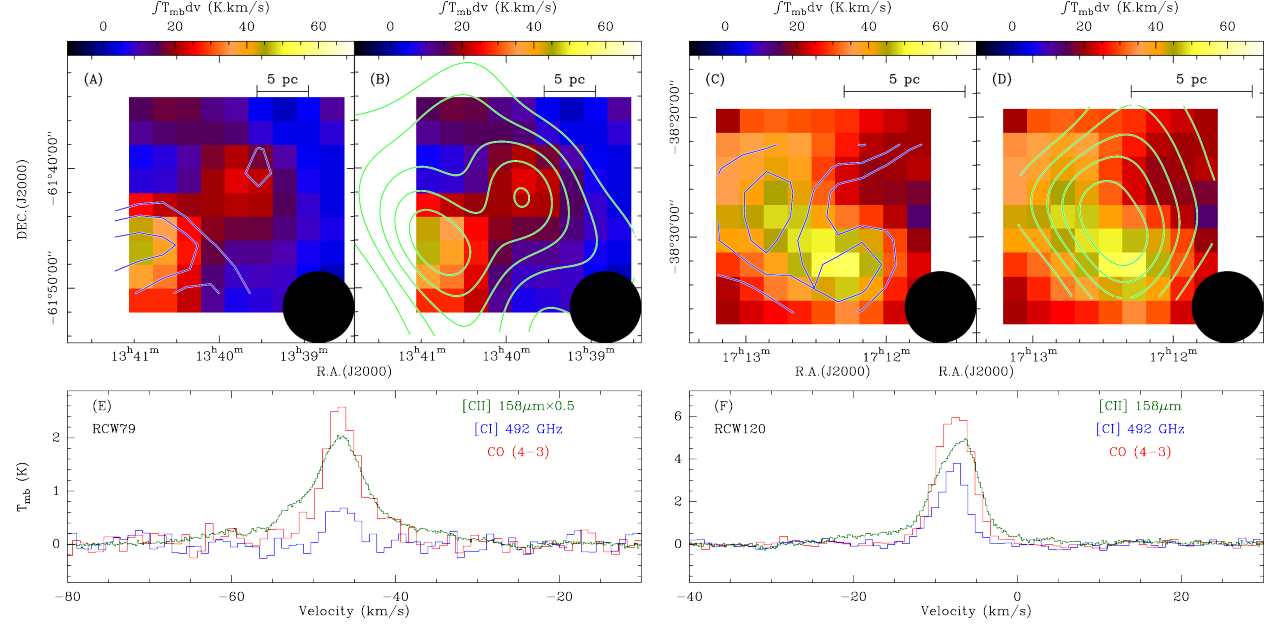


Figure 3: Distribution and spectra of \mathbf{C}^+ , \mathbf{C}^0 , and \mathbf{CO} in RCW 79 and RCW 120. (A) CO (4 – 3) integrated intensity map of RCW 79 overlaid with its [CI] integrated intensity contours (blue). The integrated velocity range for CO (4 – 3) is from -40 km s^{-1} to -30 km s^{-1} . The [CI] contours are the same as those in Figure 2. (B) Similar to panel (A) but overlaid with the [CII] integrated intensity contours (green). The integrated velocity range for [CII] is -70 km s^{-1} to -10 km s^{-1} . The contours start at 25 K km s^{-1} and increase in steps of 10 K km s^{-1} . (C) and (D) similar to (A) and (B), respectively, but for RCW 120. The CO (4–3) and [CII] integrated velocity ranges are -13 to -3 km s^{-1} and -30 to 10 km s^{-1} , respectively; [CII] contours start at 25 K km s^{-1} and increase by 10 K km s^{-1} . In panels (A)–(D), the color scale shows the CO (4–3) integrated intensity, and the beam size is indicated in the lower right corner. (E) [CII], [CI], and CO (4 – 3) spectra of RCW 79 averaged over the region indicated by the CO (4 – 3) integrated intensity map in panels (A)–(B). (F) Similar to panel (E) but for RCW 120. In panel (E), the [CII] spectrum has been scaled down for a better comparison, with the scaling factor provided in the legend. The [CII] $158 \mu\text{m}$ data are taken from the SOFIA legacy program FEEDBACK (13, 32, 42).

and RCW 120. A prominent broad line wing is clearly visible in the [CII] spectra, whereas such features are absent in both [CI] and CO (4 – 3). This distinction is also evident in the spectra of the selected targets (see Figure 4C–4F). This indicates that [CII] emission can trace a distinct velocity component insensitive to both [CI] and CO, confirming that [CII] is an excellent probe of cloud dynamics (13). In RCW 120, a blue-shifted component at $\lesssim -10 \text{ km s}^{-1}$ is detected in [CI] and [CII] (see Figure 3F) and in CO, ^{13}CO , [C I], and [C II] (Figure 4E), which likely originates from the near (front) side of the expanding shell (13). We find that the [CII]/[CI] and [CII]/CO line ratios in RCW 79 are about twice those measured in RCW 120. [CI] plays a crucial role in constraining the PDR models, as it bridges the transition between ionized and molecular gas layers and thus serves as a key diagnostic of the incident ultraviolet (UV) radiation field (see Figure S2 in the supplementary materials). These line ratios are essential for determining the physical conditions within the PDRs, including the strength of the UV radiation field and the gas density. Using the combined diagnostics of the three carbon phases, we derive radiation fields of $G_0 \sim 170 - 250$ Habing for the two regions in RCW 79 and $G_0 \sim 30$ Habing for the two regions in RCW 120 (see Table S2 and Section *PDR Models* in the supplementary materials). The modeling results are consistent with the interpretation that the elevated UV field in RCW 79 is produced by a cluster of multiple early-type O stars (42), whereas RCW 120, ionized by a single O8 V star (42), exhibits a comparatively weaker UV environment. This difference in the ionizing radiation field provides a straightforward explanation for the observed variations in the line ratios between the two regions.

Using observations of CO, ^{13}CO , and C^0 transitions, we estimate the physical properties of the selected regions in RCW 79 and RCW 120 with a non-local thermodynamic equilibrium (non-LTE) analysis. The non-LTE modeling indicates gas temperatures of 14.8–21.5 K, H_2 number densities of $> 10^3 \text{ cm}^{-3}$, ^{13}CO column densities of $\gtrsim 10^{16} \text{ cm}^{-2}$, and C^0 -to-CO abundance ratios of $\gtrsim 0.29$ (see Section *Non-LTE Analysis* in the supplementary materials). Adopting a $[\text{C}^{12}/\text{C}^{13}]$ isotope ratio of 50 (43), a typical $[\text{CO}/\text{H}_2]$ abundance of 8×10^{-5} (44), and the relation between the visual extinction and H_2 column densities (45), these cold regions are expected to have high extinction of $A_V \gtrsim 7$. Therefore, our observations reveal C^0/CO abundance ratios of $\gtrsim 0.3$ in cold and high-extinction regions ($A_V \gtrsim 7$), which is independently confirmed by analysis using Hi-GAL-based H_2 column density maps (see Section *Extinction Map* in the supplementary materials). The derived C^0/CO abundance ratios appear to substantially exceed the typical values of $\lesssim 0.2$ found both in the Milky

Way disk at similar extinctions (40, 46). In nearby spiral galaxies, C^0/CO abundance ratios are typically ~ 0.1 across most of the disks of NGC 3627 and NGC 4321, with enhancements up to ~ 1 in NGC 1808's starburst and even exceeding 1 – 5 in NGC 7469's strong active galactic nucleus environments (47). Our measured values are therefore significantly higher than the representative “normal-disk” level commonly found in the Milky Way and nearby spiral galaxies, suggesting an enhanced reservoir of atomic carbon in these regions.

Three primary scenarios may account for the elevated C^0/CO abundance ratios. One possibility is that high cosmic ray ionization rates can enhance C^0 abundances (48), but the lack of prominent cosmic ray sources in these environments makes this explanation unlikely. Alternatively, in the early stages of molecular cloud formation, the conversion from atomic to molecular gas proceeds with CO forming more slowly than C^0 , elevating the C^0/CO abundance ratio in young clouds (49). However, as the clouds examined here already host massive stars, this scenario is also disfavored. Instead, in evolved molecular clouds exposed to intense UV radiation, CO is efficiently photodissociated into C^0 by UV photons (10). The elevated C^0/CO abundance ratios in our targets are thus more plausibly explained by UV-driven CO dissociation resulting from strong UV radiation fields of nearby massive stars. Comparison with PDR models (see Section *PDR Models* in the supplementary materials) further indicates that a clumpy PDR structure is required, as it enables deep penetration of UV photons necessary to reproduce the observed abundance ratios. Therefore, the pronounced elevation in the C^0/CO abundance ratio is likely driven by enhanced photodissociation within a clumpy ISM under the influence of stellar feedback, underscoring the important role of massive stars in shaping the chemical composition of the surrounding ISM.

Prospect

Our CO (4–3) and [CI] ($^3P_1 - ^3P_0$) mapping observations of RCW 79 and RCW 120, conducted with ATE60, represent the first successful submillimeter detections from Dome A. These measurements offer a complete view of the carbon cycle in environments shaped by massive star feedback. Furthermore, Dome A is characterized by a typical winter precipitable water vapor of < 0.2 mm, as indicated by early Fourier transform spectrometer and satellite measurements (26, 27). These results demonstrate the extraordinary scientific promise of Dome A as a platform for submillimeter and

terahertz astronomy. The findings not only underscore the profound influence of stellar feedback from massive stars on the chemical compositions in their surrounding ISM, but also establish a foundation for future large-scale, high-angular-resolution surveys of key terahertz tracers (e.g., [CI], [NII], H_2D^+ , and high- J CO transitions) which can probe the cold and dynamic Universe in unprecedented detail. Building on earlier pioneering efforts at other Antarctic sites, including those from the Antarctic Submillimeter Telescope and Remote Observatory (AST/RO (50, 51, 52)) as well as the High Elevation Antarctic Terahertz telescope (HEAT (53)), this milestone further affirms the unique scientific advantages of the Antarctic plateau for studying the interplay of chemistry, radiation, and star formation in the cosmos, highlighting the importance of advancing Antarctic astronomy to fully realize its exceptional potential for submillimeter and terahertz science.

Materials and Methods

To enable submillimeter observations in the challenging Antarctic environment, ATE60 was developed with low-power consumption and a miniaturized receiver design. ATE60 was deployed to Dome A during the 41st CHINARE in the Antarctic summer (see Figure 1). This telescope was positioned at a longitude of $77^{\circ}06'38.82''$ and a latitude of $-81^{\circ}25'01.63''$, and an altitude of 4093 m. ATE60 is equipped with a single-pixel Nb-based Superconductor-Insulator-Superconductor (SIS) heterodyne receiver, operating in the double-sideband mode across the 456–504 GHz frequency range. Data processing was facilitated by fast Fourier transform spectrometers (FFTSs). The FFTSs, offering 32768 channels, cover an intermediate frequency bandwidth of 2.4 GHz. This configuration resulted in a spectral resolution of ~ 73 kHz, corresponding to a velocity spacing of $\sim 0.05 \text{ km s}^{-1}$ at 460 GHz. During operation, ATE60 requires only 1.5–2 kW of power, supplied by diesel generators housed in a dedicated power cabin that also supports the broader activities of the expedition team. Shortly after the successful relocation of ATE60, we first validated our receiver system by observing the massive star formation region NGC 6334I. The immediate detection of CO (4 – 3) and [CI] ($^3P_1 - ^3P_0$) at the expected velocities confirmed the observing capability of ATE60. Building on this success, we subsequently conducted CO (4 – 3) and [CI] ($^3P_1 - ^3P_0$) observations toward RCW 79 and RCW 120 between 6 and 17 January 2025, during the expedition at the Dome A site.

Based on skydip measurements taken during the observations, the typical atmospheric optical

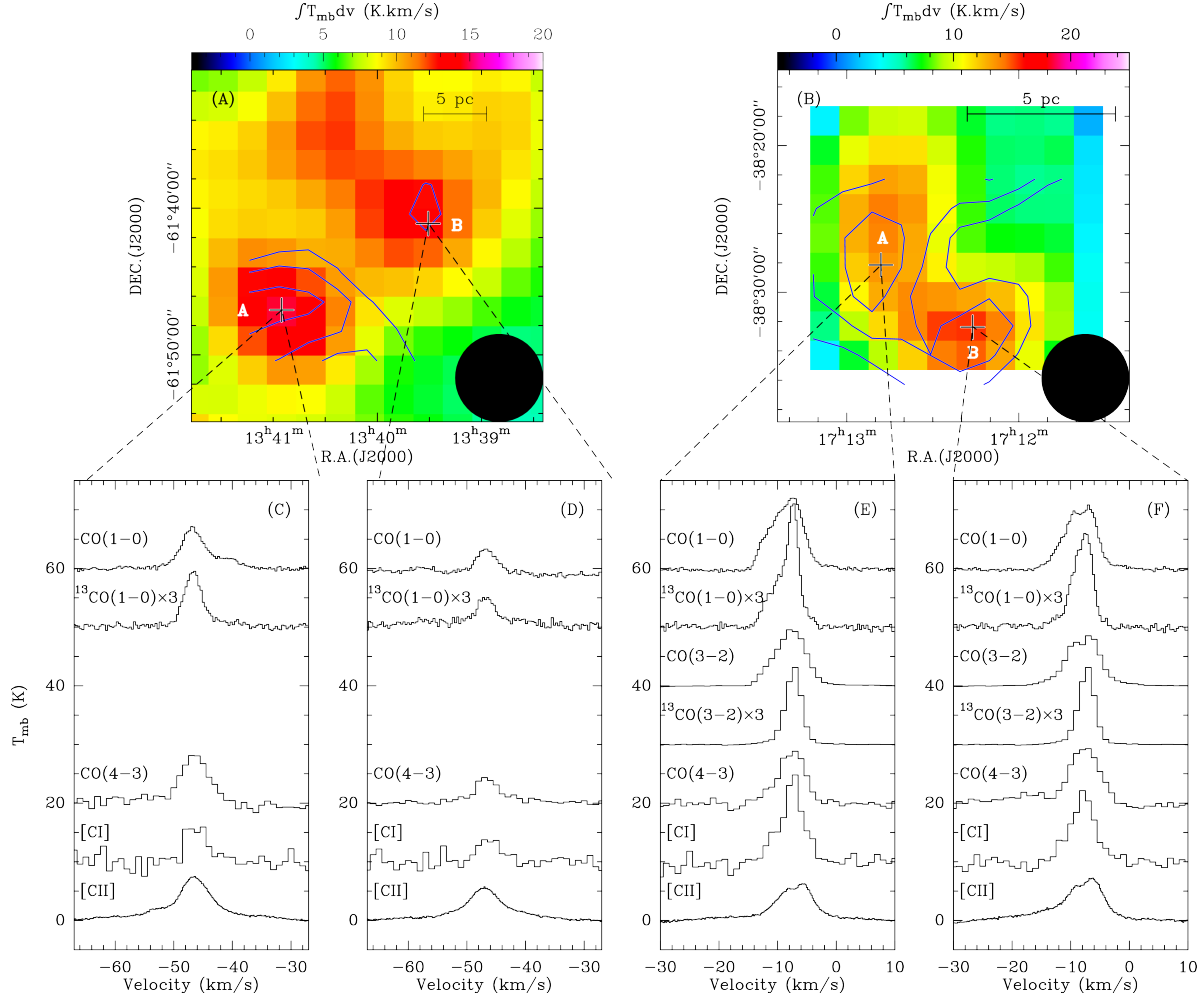


Figure 4: Observed spectra of the selected targets. (A) Integrated-intensity map of ^{13}CO (1 – 0) overlaid with [CI] contours for RCW 79. The ^{13}CO (1 – 0) integrated velocity range is from -60 km s^{-1} to -30 km s^{-1} . (B) Integrated-intensity map of ^{13}CO (3 – 2) overlaid with [CI] contours for RCW 120. The ^{13}CO (3 – 2) integrated velocity range is from -13 km s^{-1} to -3 km s^{-1} . In panels (A) and (B), the beam sizes are indicated in the lower right corner and the [CI] contours are the same as in Figure 3. Panels (C)–(F) present observed spectra of the selected targets which are extracted from the pixels indicated by pluses in panels (A) and (B). The transitions are labeled in each panel and the ^{13}CO transitions are scaled by a factor of 3 for comparison.

depth at 460 GHz is ~ 0.5 , corresponding to a precipitable water vapor (PWV) of ~ 1 mm. These conditions are comparable to the median PWV value (~ 1.2 mm) during the Bolivian winter at Llano de Chajnantor, the site of the Atacama Pathfinder EXperiment (APEX) and Atacama Large Millimeter/submillimeter Array (54). The two-load (hot and cold) calibration was used to set the antenna temperature scale. During the observations, ambient temperatures were about 240 K (i.e., -33°C). The receiver temperatures were about 600 K and 300 K, with the corresponding atmosphere-corrected system temperatures estimated at 1093–3921 K and 1120–3750 K at 462 GHz and 493 GHz, respectively. The absolute flux calibration uncertainties were assumed to be 20% (see Section *Flux Calibration* in the supplementary materials). The half-power beam widths (HPBWs) were measured to be approximately $270''$ and $240''$ at 460 GHz and 492 GHz, respectively. The overall pointing error was estimated to be $\lesssim 1'$ (see Section *Pointing* in the supplementary materials).

After initial mapping of RCW 79 and RCW 120, we observed that RCW 120 exhibits brighter [CI] (${}^3P_1 - {}^3P_0$) emission compared to RCW 79 (see Figure 3). Consequently, we prioritized our ATE60 CI observations on RCW 120 to improve sensitivity. To enhance the signal-to-noise ratio, we smoothed the spectra to a velocity spacing of 1 km s^{-1} , and the noise level of [CI] data at this channel width is ~ 0.15 K for RCW 79 and ~ 0.12 K for RCW 120 on the antenna temperature scale.

References and Notes

1. K. Lodders, Solar System Abundances and Condensation Temperatures of the Elements. *The Astrophysical Journal* **591** (2), 1220–1247 (2003), doi:10.1086/375492.
2. T. Henning, F. Salama, Carbon in the Universe. *Science* **282**, 2204 (1998), doi:10.1126/science.282.5397.2204.
3. T. M. Dame, D. Hartmann, P. Thaddeus, The Milky Way in Molecular Clouds: A New Complete CO Survey. *The Astrophysical Journal* **547** (2), 792–813 (2001), doi:10.1086/318388.
4. A. D. Bolatto, M. Wolfire, A. K. Leroy, The CO-to-H₂ Conversion Factor. *Annual Review of Astronomy and Astrophysics* **51** (1), 207–268 (2013), doi:10.1146/annurev-astro-082812-140944.
5. Y. Su, *et al.*, The Milky Way Imaging Scroll Painting (MWISP): Project Details and Initial Results from the Galactic Longitudes of 25.[°]8-49.[°]7. *The Astrophysical Journal Supplement Series* **240** (1), 9 (2019), doi:10.3847/1538-4365/aaf1c8.
6. I. A. Grenier, J.-M. Casandjian, R. Terrier, Unveiling Extensive Clouds of Dark Gas in the Solar Neighborhood. *Science* **307** (5713), 1292–1295 (2005), doi:10.1126/science.1106924.
7. Planck Collaboration, *et al.*, Planck early results. XIX. All-sky temperature and dust optical depth from Planck and IRAS. Constraints on the “dark gas” in our Galaxy. *Astronomy & Astrophysics* **536**, A19 (2011), doi:10.1051/0004-6361/201116479.
8. M. G. Wolfire, D. Hollenbach, C. F. McKee, The Dark Molecular Gas. *The Astrophysical Journal* **716** (2), 1191–1207 (2010), doi:10.1088/0004-637X/716/2/1191.
9. E. F. van Dishoeck, J. H. Black, The Photodissociation and Chemistry of Interstellar CO. *The Astrophysical Journal* **334**, 771 (1988), doi:10.1086/166877.
10. D. J. Hollenbach, A. G. G. M. Tielens, Photodissociation regions in the interstellar medium of galaxies. *Reviews of Modern Physics* **71** (1), 173–230 (1999), doi:10.1103/RevModPhys.71.173.

11. M. G. Wolfire, L. Vallini, M. Chevance, Photodissociation and X-Ray-Dominated Regions. *Annual Review of Astronomy and Astrophysics* **60**, 247–318 (2022), doi:10.1146/annurev-astro-052920-010254.
12. C. Pabst, *et al.*, Disruption of the Orion molecular core 1 by wind from the massive star θ^1 Orionis C. *Nature* **565** (7741), 618–621 (2019), doi:10.1038/s41586-018-0844-1.
13. M. Luisi, *et al.*, Stellar feedback and triggered star formation in the prototypical bubble RCW 120. *Science Advances* **7** (15), eabe9511 (2021), doi:10.1126/sciadv.abe9511.
14. N. Schneider, *et al.*, Ionized carbon as a tracer of the assembly of interstellar clouds. *Nature Astronomy* **7**, 546–556 (2023), doi:10.1038/s41550-023-01901-5.
15. C. Heiles, On the Origin of the Diffuse C + 158 Micron Line Emission. *The Astrophysical Journal* **436**, 720 (1994), doi:10.1086/174945.
16. J. L. Pineda, W. D. Langer, T. Velusamy, P. F. Goldsmith, A Herschel [C ii] Galactic plane survey. I. The global distribution of ISM gas components. *Astronomy & Astrophysics* **554**, A103 (2013), doi:10.1051/0004-6361/201321188.
17. M. Röllig, *et al.*, [C II] 158 μ m and [N II] 205 μ m emission from IC 342. Disentangling the emission from ionized and photo-dissociated regions. *Astronomy & Astrophysics* **591**, A33 (2016), doi:10.1051/0004-6361/201526267.
18. P. P. Papadopoulos, W. F. Thi, S. Viti, CI lines as tracers of molecular gas, and their prospects at high redshifts. *Monthly Notices of the Royal Astronomical Society* **351** (1), 147–160 (2004), doi:10.1111/j.1365-2966.2004.07762.x.
19. S. S. R. Offner, T. G. Bisbas, T. A. Bell, S. Viti, An alternative accurate tracer of molecular clouds: the ‘XCi-factor’. *Monthly Notices of the Royal Astronomical Society* **440**, L81–L85 (2014), doi:10.1093/mnrasl/slu013.
20. S. C. O. Glover, P. C. Clark, M. Micic, F. Molina, Modelling [C I] emission from turbulent molecular clouds. *Monthly Notices of the Royal Astronomical Society* **448** (2), 1607–1627 (2015), doi:10.1093/mnras/stu2699.

21. M. Y. Lee, F. Wyrowski, K. Menten, M. Tiwari, R. Güsten, ATLASGAL-selected massive clumps in the inner Galaxy. X. Observations of atomic carbon at 492 GHz. *Astronomy & Astrophysics* **664**, A80 (2022), doi:10.1051/0004-6361/202142404.
22. G. J. Stacey, *et al.*, CCAT-Prime: science with an ultra-widefield submillimeter observatory on Cerro Chajnantor, in *Ground-based and Airborne Telescopes VII*, H. K. Marshall, J. Spyromilio, Eds., vol. 10700 of *Society of Photo-Optical Instrumentation Engineers (SPIE) Conference Series* (2018), p. 107001M, doi:10.1117/12.2314031.
23. T. K. Sridharan, *et al.*, A Prospective ISRO-CfA Himalayan Sub-millimeter-wave Observatory Initiative. *arXiv e-prints* arXiv:2008.07453 (2020), doi:10.48550/arXiv.2008.07453.
24. M. G. Burton, Astronomy in Antarctica. *Astronomy and Astrophysics Review* **18** (4), 417–469 (2010), doi:10.1007/s00159-010-0032-2.
25. H. Yang, *et al.*, Exceptional Terahertz Transparency and Stability above Dome A, Antarctica. *Publications of the Astronomical Society of the Pacific* **122** (890), 490 (2010), doi:10.1086/652276.
26. S.-C. Shi, *et al.*, Terahertz and far-infrared windows opened at Dome A in Antarctica. *Nature Astronomy* **1**, 0001 (2016), doi:10.1038/s41550-016-0001.
27. C.-L. Kuo, Assessments of Ali, Dome A, and Summit Camp for mm-wave Observations Using MERRA-2 Reanalysis. *The Astrophysical Journal* **848** (1), 64 (2017), doi:10.3847/1538-4357/aa8b74.
28. H. Matsuo, S.-C. Shi, S. Paine, Q.-J. Yao, Z.-H. Lin, Terahertz Atmospheric Windows for High Angular Resolution Terahertz Astronomy from Dome A. *arXiv e-prints* arXiv:1902.06398 (2019), doi:10.48550/arXiv.1902.06398.
29. C. A. Kulesa, *et al.*, Pre-HEAT: submillimeter site testing and astronomical spectra from Dome A, Antarctica, in *Ground-based and Airborne Telescopes II*, L. M. Stepp, R. Gilmozzi, Eds., vol. 7012 of *Society of Photo-Optical Instrumentation Engineers (SPIE) Conference Series* (2008), p. 701249, doi:10.1117/12.789741.

30. Z. Shang, Astronomy from Dome A in Antarctica. *Research in Astronomy and Astrophysics* **20** (10), 168 (2020), doi:10.1088/1674-4527/20/10/168.

31. J. Li, *et al.*, Terahertz Science and Technology in Astronomy, Telecommunications, and Biophysics. *Research* **8**, 0586 (2025), doi:10.34133/research.0586, <https://spj.science.org/doi/abs/10.34133/research.0586>.

32. L. Bonne, *et al.*, The SOFIA FEEDBACK [CII] Legacy Survey: Rapid molecular cloud dispersal in RCW 79. *Astronomy & Astrophysics* **679**, L5 (2023), doi:10.1051/0004-6361/202347721.

33. K. Torii, *et al.*, Cloud-Cloud Collision as a Trigger of the High-mass Star Formation: a Molecular Line Study in RCW120. *The Astrophysical Journal* **806** (1), 7 (2015), doi:10.1088/0004-637X/806/1/7.

34. M. Figueira, *et al.*, Star formation towards the Galactic H II region RCW 120. Herschel observations of compact sources. *Astronomy & Astrophysics* **600**, A93 (2017), doi:10.1051/0004-6361/201629379.

35. A. Ohama, *et al.*, The formation of a Spitzer bubble RCW 79 triggered by a cloud-cloud collision. *Publications of the Astronomical Society of Japan* **70**, S45 (2018), doi:10.1093/pasj/psy025.

36. S. Kabanovic, *et al.*, Self-absorption in [C II], ^{12}CO , and H I in RCW120. Building up a geometrical and physical model of the region. *Astronomy & Astrophysics* **659**, A36 (2022), doi:10.1051/0004-6361/202142575.

37. A. Zavagno, *et al.*, Triggered massive-star formation on the borders of Galactic H II regions. II. Evidence for the collect and collapse process around RCW 79. *Astronomy & Astrophysics* **446** (1), 171–184 (2006), doi:10.1051/0004-6361:20053952.

38. A. Zavagno, *et al.*, Triggered star formation on the borders of the Galactic H ii region RCW 120. *Astronomy & Astrophysics* **472** (3), 835–846 (2007), doi:10.1051/0004-6361:20077474.

39. H.-L. Liu, *et al.*, Herschel observations of the Galactic H II region RCW 79. *Astronomy & Astrophysics* **602**, A95 (2017), doi:10.1051/0004-6361/201629915.

40. M. Ikeda, *et al.*, Large-Scale Mapping Observations of the C I ($^3\text{P}_1$ - $^3\text{P}_0$) and CO ($J = 3-2$) Lines toward the Orion A Molecular Cloud. *The Astrophysical Journal Letters* **527** (1), L59–L62 (1999), doi:10.1086/312395.

41. Y. Shimajiri, *et al.*, Extensive [C I] Mapping toward the Orion-A Giant Molecular Cloud. *The Astrophysical Journal Letters* **774** (2), L20 (2013), doi:10.1088/2041-8205/774/2/L20.

42. N. Schneider, *et al.*, FEEDBACK: a SOFIA Legacy Program to Study Stellar Feedback in Regions of Massive Star Formation. *Publications of the Astronomical Society of the Pacific* **132** (1016), 104301 (2020), doi:10.1088/1538-3873/aba840.

43. Y. T. Yan, *et al.*, Direct measurements of carbon and sulfur isotope ratios in the Milky Way. *Astronomy & Astrophysics* **670**, A98 (2023), doi:10.1051/0004-6361/202244584.

44. M. A. Frerking, W. D. Langer, R. W. Wilson, The relationship between carbon monoxide abundance and visual extinction in interstellar clouds. *The Astrophysical Journal* **262**, 590–605 (1982), doi:10.1086/160451.

45. R. C. Bohlin, B. D. Savage, J. F. Drake, A survey of interstellar H I from Lalpha absorption measurements. II. *The Astrophysical Journal* **224**, 132–142 (1978), doi:10.1086/156357.

46. T. Sakai, T. Oka, S. Yamamoto, Atomic Carbon in the AFGL 333 Cloud. *The Astrophysical Journal* **649** (1), 268–279 (2006), doi:10.1086/504861.

47. D. Liu, *et al.*, C I and CO in nearby spiral galaxies. I. Line ratio and abundance variations at ~ 200 pc scales. *Astronomy & Astrophysics* **672**, A36 (2023), doi:10.1051/0004-6361/202244564.

48. T. G. Bisbas, P. P. Papadopoulos, S. Viti, Effective Destruction of CO by Cosmic Rays: Implications for Tracing H₂ Gas in the Universe. *The Astrophysical Journal* **803** (1), 37 (2015), doi:10.1088/0004-637X/803/1/37.

49. E. A. Bergin, L. W. Hartmann, J. C. Raymond, J. Ballesteros-Paredes, Molecular Cloud Formation behind Shock Waves. *The Astrophysical Journal* **612** (2), 921–939 (2004), doi:10.1086/422578.

50. A. A. Stark, *et al.*, First Detection of 492 GHz [C I] Emission from the Large Magellanic Cloud. *The Astrophysical Journal Letters* **480** (1), L59–L62 (1997), doi:10.1086/310618.

51. R. Ojha, *et al.*, AST/RO Observations of Atomic Carbon near the Galactic Center. *The Astrophysical Journal* **548** (1), 253–257 (2001), doi:10.1086/318693.

52. X. Zhang, Y. Lee, A. Bolatto, A. A. Stark, CO (J=4–3) and [C I] Observations of the Carina Molecular Cloud Complex. *The Astrophysical Journal* **553** (1), 274–287 (2001), doi:10.1086/320628.

53. M. G. Burton, *et al.*, Extended Carbon Line Emission in the Galaxy: Searching for Dark Molecular Gas along the G328 Sightline. *The Astrophysical Journal* **811** (1), 13 (2015), doi:10.1088/0004-637X/811/1/13.

54. R. Güsten, *et al.*, The Atacama Pathfinder EXperiment (APEX) - a new submillimeter facility for southern skies -. *Astronomy & Astrophysics* **454** (2), L13–L16 (2006), doi:10.1051/0004-6361:20065420.

55. P. J. Barnes, D. G. H. Barnes, A. K. Hernández, S. Lopez, E. Muller, The Three-mm Ultimate Mopra Milky Way Survey. III. Data Release 6, An Atlas of Physical Conditions, Global Mass Conversion Laws, and 3D Physical Architecture of the Molecular Interstellar Medium in the Fourth Quadrant. *The Astrophysical Journal Supplement Series* **280** (1), 31 (2025), doi:10.3847/1538-4365/adf32b.

56. S. Goedhart, *et al.*, The SARAO MeerKAT 1.3 GHz Galactic Plane Survey. *Monthly Notices of the Royal Astronomical Society* **531** (1), 649–681 (2024), doi:10.1093/mnras/stae1166.

57. R. A. Benjamin, *et al.*, GLIMPSE. I. An SIRTF Legacy Project to Map the Inner Galaxy. *Publications of the Astronomical Society of the Pacific* **115** (810), 953–964 (2003), doi:10.1086/376696.

58. S. J. Carey, *et al.*, MIPSGAL: A Survey of the Inner Galactic Plane at 24 and 70 μ m. *Publications of the Astronomical Society of the Pacific* **121** (875), 76 (2009), doi:10.1086/596581.

59. K. A. Marsh, A. P. Whitworth, O. Lomax, Temperature as a third dimension in column-density mapping of dusty astrophysical structures associated with star formation. *Monthly Notices of the Royal Astronomical Society* **454** (4), 4282–4292 (2015), doi:10.1093/mnras/stv2248.

60. K. A. Marsh, *et al.*, Multitemperature mapping of dust structures throughout the Galactic Plane using the PPMAP tool with Herschel Hi-GAL data. *Monthly Notices of the Royal Astronomical Society* **471** (3), 2730–2742 (2017), doi:10.1093/mnras/stx1723.

61. E. Keilmann, *et al.*, [C II]-deficit caused by self-absorption in an ionized carbon-filled bubble in RCW79. *Astronomy & Astrophysics* **697**, L2 (2025), doi:10.1051/0004-6361/202453445.

62. M. A. Kuhn, L. A. Hillenbrand, A. Sills, E. D. Feigelson, K. V. Getman, Kinematics in Young Star Clusters and Associations with Gaia DR2. *The Astrophysical Journal* **870** (1), 32 (2019), doi:10.3847/1538-4357/aaef8c.

63. F. F. S. van der Tak, J. H. Black, F. L. Schöier, D. J. Jansen, E. F. van Dishoeck, A computer program for fast non-LTE analysis of interstellar line spectra. With diagnostic plots to interpret observed line intensity ratios. *Astronomy & Astrophysics* **468** (2), 627–635 (2007), doi:10.1051/0004-6361:20066820.

64. F. F. S. van der Tak, F. Lique, A. Faure, J. H. Black, E. F. van Dishoeck, The Leiden Atomic and Molecular Database (LAMDA): Current Status, Recent Updates, and Future Plans. *Atoms* **8** (2), 15 (2020), doi:10.3390/atoms8020015.

65. D. A. Neufeld, *et al.*, Spitzer Observations of HH 54 and HH 7-11: Mapping the H₂ Ortho-to-Para Ratio in Shocked Molecular Gas. *The Astrophysical Journal* **649** (2), 816–835 (2006), doi:10.1086/506604.

66. M. J. Reid, *et al.*, Trigonometric Parallaxes of High-mass Star-forming Regions: Our View of the Milky Way. *The Astrophysical Journal* **885** (2), 131 (2019), doi:10.3847/1538-4357/ab4a11.

67. D. Foreman-Mackey, D. W. Hogg, D. Lang, J. Goodman, emcee: The MCMC Hammer. *Publications of the Astronomical Society of the Pacific* **125** (925), 306 (2013), doi:10.1086/670067.

68. J. Goodman, J. Weare, Ensemble samplers with affine invariance. *Communications in Applied Mathematics and Computational Science* **5** (1), 65–80 (2010), doi:10.2140/camcos.2010.5.65.

69. M. Röllig, R. Szczerba, V. Ossenkopf, C. Glück, Full SED fitting with the KOSMA- τ PDR code. I. Dust modelling. *Astronomy & Astrophysics* **549**, A85 (2013), doi:10.1051/0004-6361/201118190.

70. M. Röllig, V. Ossenkopf-Okada, The KOSMA- τ PDR model. I. Recent updates to the numerical model of photo-dissociated regions. *Astronomy & Astrophysics* **664**, A67 (2022), doi:10.1051/0004-6361/202141854.

71. M. W. Pound, M. G. Wolfire, The PhotoDissociation Region Toolbox: Software and Models for Astrophysical Analysis. *The Astronomical Journal* **165** (1), 25 (2023), doi:10.3847/1538-3881/ac9b1f.

72. S. Ishii, *et al.*, Large-scale CO (J = 4-3) mapping toward the Orion-A giant molecular cloud. *Publications of the Astronomical Society of Japan* **68** (1), 10 (2016), doi:10.1093/pasj/psv116.

Acknowledgments

We thank Xinmiao Jin, Bin Ma, Chao Chen, and all members of the 41st CHINARE for their strong support in carrying out the observations at Dome A. The MeerKAT telescope is operated by the South African Radio Astronomy Observatory, which is a facility of the National Research Foundation, an agency of the Department of Science and Innovation.

Funding: This work was supported by the Strategic Priority Research Program of the Chinese Academy of Sciences (Grant No. XDB0800000) and the National Key Research and Development Program of China (Grant No. 2023YFA1608200). We also acknowledge support from the National Natural Science Foundation of China (NSFC) under Grants No. 12222308 and 12333013.

Author contributions: Writing – original draft: Y.G., W.Z., W.M., J.Liu, Z.W., K.Z., B.L.L., X.M.L., S.M.X., Y.J.L., X.J.D., J.J., L.L., L.G., Y.Z., and J.Li

Writing - review & editing: Y.G., J.Q.Z., Y.R., Y.L.Z., D.Z.L., Y.P.A., Q.J.Y., W.Z., W.M., Z.H.L.,

D.L., K.M.Z., J.Liu, Z.W., J.D.J., K.Z., F.W., J.P.L., B.L.L., X.Z., Z.H.L., J.M.W., H.Q.H., X.M.L., S.M.X., J.Q., Y.J.L., J.T.L., X.J.D., J.J., L.L., L.G., P.J., Y.Z., C.G.S., S.N., R.Q.M., S.C.S., J.Li
Data curation: Y.G., J.Q.Z., Y.R., Y.L.Z., D.Z.L., W.Z., W.M., J.Liu, Z.W., K.Z., F.W., X.Z., X.M.L., S.M.X., Y.J.L., L.L., L.G., Y.Z., S.N., and J.Li

Formal analysis: Y.G., Y.R., D.Z.L., W.Z., W.M., J.Liu, Z.W., K.Z., F.W., J.P.L., B.L.L., X.Z., X.M.L., S.M.X., Y.J.L., L.L., L.G., Y.Z., S.N., and J.Li

Visualization: Y.G., J.Q.Z., W.Z., W.M., J.Liu, Z.W., K.Z., F.W., B.L.L., X.Z., X.M.L., S.M.X., Y.J.L., J.T.L., L.L., L.G., Y.Z., S.N., and J.Li

Investigation: Y.G., J.Q.Z., Y.R., Y.L.Z., D.Z.L., Q.J.Y., W.Z., W.M., D.L., J.Liu, Z.W., J.D.J., K.Z., F.W., B.L.L., X.Z., X.M.L., S.M.X., Y.J.L., J.T.L., J.J., L.L., L.G., T.J., P.J., Y.Z., S.N., and J.Li

Methodology: Y.G., J.Q.Z., Y.R., D.Z.L., Q.J.Y., W.Z., W.M., W.Y.D., D.L., J.Liu, Z.W., K.Z., F.W., J.P.L., B.L.L., H.Q.H., X.M.L., S.M.X., J.T.L., X.J.D., J.J., L.L., L.G., Y.Z., S.N., S.C.S., and J.Li

Resources: Y.G., J.Q.Z., Y.R., D.Z.L., Q.J.Y., W.Z., W.M., Z.H.L., W.Y.D., K.M.Z., J.Liu, Z.W., J.D.J., K.Z., F.W., B.L.L., H.Q.H., X.M.L., S.M.X., Y.J.L., J.T.L., X.J.D., L.L., L.G., T.J., P.J., Y.Z., S.N., S.C.S., and J.Li

Software: Y.G., J.Q.Z., Y.R., D.Z.L., Q.J.Y., W.Z., W.M., Z.H.L., W.Y.D., J.Liu, K.Z., F.W., X.M.L., S.M.X., L.L., L.G., Y.Z., and J.Li

Conceptualization: Y.G., J.Q.Z., Y.R., D.Z.L., Q.J.Y., W.Z., W.M., D.L., J.Liu, Z.W., K.Z., F.W., X.M.L., S.M.X., J.T.L., X.J.D., J.J., L.L., L.G., P.J., Y.Z., R.Q.M., S.C.S., and J.Li

Validation: Y.G., J.Q.Z., Y.R., D.Z.L., Q.J.Y., W.Z., W.M., Z.H.L., D.L., J.Liu, Z.W., K.Z., F.W., J.P.L., B.L.L., X.Z., J.M.W., H.Q.H., X.M.L., S.M.X., J.Q., Y.J.L., J.T.L., L.L., L.G., Y.Z., C.G.S., S.N., and J.Li

Supervision: R.Q.M., S.C.S., and J.Li

Project administration: P.J., S.C.S., and J.Li

Funding acquisition: D.Z.L., C.G.S., R.Q.M., S.C.S., and J.Li

Competing interests: There are no competing interests to declare.

Data and materials availability: The reduced ATE60 CO (4 – 3) and [CI] data cubes are available on Zenodo at <https://doi.org/10.5281/zenodo.17410999>. The ^{12}CO (1 – 0), ^{13}CO (1 – 0), and C^{18}O (1 – 0) data from the Three-mm Ultimate Mopra Milky Way Survey are available at <https://gemelli.spacescience.org/~pbarnes/research/thrumms/rbank/>. The APEX ^{12}CO (3 – 2) and ^{13}CO (3 – 2) data are available at the CDS archive (<http://cdsarc.u-strasbg.fr/viz-bin/cat/J/A+A/659/A36>). The [CII] data are provided at the NASA/IPAC Infrared science archive (<https://irsa.ipac.caltech.edu/applications/sofia>). The 1.3 GHz radio continuum data are provided at the SARAQ Data Archive (<https://archive-gw-1.kat.ac.za/public/repository/10.48479/3wfd-e270/index.html>). The GLIMPSE 8 μm and MIPSGAL 24 μm data are available at the NASA/IPAC infrared science archive (<https://irsa.ipac.caltech.edu/Missions/spitzer.html>). The H_2 column density maps derived from the Herschel Hi-GAL data are provided at <http://www.astro.cardiff.ac.uk/research/ViaLactea/>. The codes used for the ATE telescopes are publicly available via Zenodo (<https://doi.org/10.5281/zenodo.17410999>).

Supplementary materials

Supplementary Text

Figs. S1 to S7

Tables S1 to S2

Supplementary Materials for

First Submillimeter Lights from Dome A: Tracing the Carbon Cycle in the Feedback of Massive Stars

Yan Gong^{1†}, Jiaqiang Zhong^{1,3†}, Yuan Ren^{1,3}, Yilong Zhang^{1,3}, Daizhong Liu¹,
Yiping Ao^{1,3}, Qijun Yao¹, Wen Zhang^{1,3}, Wei Miao^{1,3}, Zhenhui Lin^{1,3},
Wenying Duan^{1,2}, Dong Liu¹, Kangmin Zhou¹, Jie Liu¹, Zheng Wang¹, Junda Jin¹,
Kun Zhang¹, Feng Wu¹, Jinpeng Li¹, Boliang Liu¹, Xuan Zhang^{1,3}, Zhengheng Luo^{1,2},
Jiameng Wang^{1,2}, Huiqian Hao⁴, Xingming Lu⁴, Shaoming Xie⁴, Jia Quan⁵,
Yanjie Liu⁵, Jingtao Liang⁵, Xianjin Deng^{6,7}, Jun Jiang^{6,7}, Li Li^{6,7},
Liang Guo⁸, Tuo Ji⁹, Peng Jiang⁹, Yi Zhang¹⁰, Chenggang Shu¹⁰,
Sudeep Neupane¹¹, Ruiqing Mao¹, Shengcai Shi¹, Jing Li^{1*}

¹ Purple Mountain Observatory and Key Laboratory of Radio Astronomy, Chinese Academy of Sciences, Nanjing 210008, China ² School of Astronomy and Space Sciences, University of Science and Technology of China, Hefei 230026, China ³ State Key Laboratory of Radio Astronomy and Technology, National Astronomical Observatories, Chinese Academy of Sciences, Beijing 100101, China ⁴ The 54th Research

Institute of China Electronics Technology Group Corporation, Shijiazhuang 050081, China ⁵ Technical Institute of Physics and Chemistry, Chinese Academy of Sciences, Beijing 100190, China ⁶ Microsystem and Terahertz Research Center, China Academy of Engineering Physics, Chengdu, Sichuan 610200, China

⁷ Institute of Electronic Engineering, China Academy of Engineering Physics, Mianyang, Sichuan 621999, China ⁸ Changchun Institute of Optics, Fine Mechanics and Physics, Chinese Academy of Sciences, Changchun 130033, China ⁹ Polar Research Institute of China; Key Laboratory for Polar Science, MNR, Shanghai 200136, China ¹⁰ Shanghai Key Lab for Astrophysics, Shanghai Normal University, 100 Guilin Road, Shanghai 200234, China ¹¹ Max-Planck-Institut für Radioastronomie, Auf dem Hügel 69, D-53121 Bonn, Germany *Corresponding author. Email: lijing@pmo.ac.cn [†]These authors contributed equally to

this work.

This PDF file includes:

Supplementary Text

Figures S1 to S7

Tables S1 to S2

Supplementary Text

Archival Data

- **[CII] 158 μ m data.** We retrieve the [CII] 158 μ m data of RCW 120 and RCW 79 from the SOFIA legacy program FEEDBACK (42). These [CII] observations were obtained using the upGREAT heterodyne spectrometer onboard SOFIA. The archival data have a HPBW of 14.''1 and a channel width is 0.2 km s^{-1} . The absolute flux calibration uncertainties were assumed to be 10% for the [CII] data.
- **Low- J CO data.** Both RCW 120 and RCW 79 have been extensively mapped in low- J CO transitions. For both regions, the ^{12}CO (1 – 0) and ^{13}CO (1 – 0) data are taken from the data release 6 products of the Three-mm Ultimate Mopra Milky Way Survey (55) with an HPBW of 72''. For RCW 120, additional ^{12}CO (3 – 2) and ^{13}CO (3 – 2) observations were obtained with APEX (36), providing a higher angular resolution with an HPBW of 20''. The absolute flux calibration uncertainties were assumed to be 10% for the low- J CO data.
- **Radio continuum data.** The 1.3 GHz radio continuum image of RCW 120 and RCW 79 were taken from the first data release (DR1) of the SARA0 MeerKAT Galactic Plane Survey (56), providing an angular resolution of 8''.
- **Infrared data.** The Spitzer 8 μ m and 24 μ m data were taken from the Galactic Legacy Infrared Mid-Plane Survey Extraordinaire (GLIMPSE (57)) and the Multiband Imaging Photometer for Spitzer Galactic Plane Survey (MIPSGAL (58)). Their angular resolutions are 1.''9 and 6'', respectively.
- **Hi-GAL based H_2 column density maps.** The H_2 column density maps were generated by applying the point process mapping (PPMAP) technique (59) to multi-wavelength Herschel imaging data, enabling the construction of high-resolution, dust temperature–resolved column density distributions across the Galactic plane (60). The Hi-GAL based H_2 column density maps achieve an angular resolution of 12''.

Source Selection

In the SOFIA FEEDBACK survey (42), RCW 79 and RCW 120 stand out as the only two sources exhibiting prominent, well-defined ring-like morphologies in their PDRs (see Figure 2). This striking structure provides compelling evidence that the surrounding gas has been profoundly reshaped by the feedback from massive stars. Both regions exhibit clear interactions between molecular clouds and H_{II} regions, with previous studies suggesting that triggered star formation occurs in their peripheries (37, 38, 39). Intense UV radiation from massive stars likely drives photodissociation at the edges of these H_{II} regions, making them ideal sites for studying the transition between different carbon phases. While both regions have been extensively studied in CO and [CII] emission (32, 33, 13, 34, 35, 36, 61), [CI] observations are absent. Our ATE60 [CI] observations can address this crucial gap, enabling a more comprehensive study of the carbon cycle in these environments. RCW 79 and RCW 120 are located at a distance of \sim 4 kpc (32) and \sim 1.7 kpc (62), respectively. Their large angular sizes of $\gtrsim 10'$ allow for spatially resolved observations with ATE60. Situated in the circumpolar sky as seen from Dome A, both sources are accessible for long-duration observations, making them ideal targets for this study.

Non-LTE Analysis

To enhance the signal-to-noise ratios, all datasets were first convolved to a common HPBW of 6'. We selected four bright positions for a detailed analysis of their physical properties, and the corresponding spectra are presented in Figure 4. A single-component Gaussian profile was fitted to the spectral data to derive the observed parameters of most lines, whereas a two-component Gaussian profile was used to fit the [CII] spectra. The derived parameters are summarized in Table S1.

In order to derive the physical properties of the selected regions, we use the non-local thermodynamic equilibrium (non-LTE) radiative transfer code RADEX¹ for the calculations (63). In our calculations, we assume that CO, ¹³CO, and C⁰ transitions trace gas with the same gas temperature and H₂ number density, so their transitions can be simultaneously modeled. The information on energy levels, statistical weights, Einstein A-coefficients and collisional rate coefficients of CO, ¹³CO, and

¹<https://home.strw.leidenuniv.nl/~moldata/radex.html>

C^0 transitions is directly taken from the Leiden Atomic and Molecular Database (LAMDA²) (64). During our modeling, we used the classic large-velocity gradient (LVG) approximation to estimate the escape probability. Based on previous studies (65), a constant H_2 ortho-to-para ratio of 0.25 is assumed in this study. The line widths are taken to be the fitted values of respective transitions (see Table S1).

To reduce the number of the free parameters, we assume that the $[\text{CO}^{12}/\text{CO}^{13}]$ abundance ratio approximates the $[\text{C}^{12}/\text{C}^{13}]$ isotope ratio. The Galactocentric distance, R_{gc} , was calculated using the expression

$$R_{\text{gc}} = \sqrt{R_{\text{gc}, \odot}^2 + d^2 - 2R_{\text{gc}, \odot}d\cos(l)}, \quad (\text{S1})$$

where $R_{\text{gc}, \odot} = 8.15$ kpc is the Galactocentric distance of the Sun (66), d is the heliocentric distance of the source, and l is the Galactic longitude. For RCW 79 and RCW 120, we adopted a heliocentric distance of ~ 4 kpc (32) and ~ 1.7 kpc (62), respectively, which yields Galactocentric distances of ~ 6.5 kpc for both regions. Assuming that the $[\text{C}^{12}/\text{C}^{13}]$ isotope ratio follows the gradient $^{12}\text{C}/^{13}\text{C} = 4.77R_{\text{gc}} + 20.76$ (43), we used a representative $[\text{CO}^{12}/\text{CO}^{13}]$ abundance ratio of 50 in this work.

We performed parameter estimation using the *emcee* package (67), which implements the affine-invariant ensemble sampler (68) for the Markov chain Monte Carlo (MCMC) approach. This approach allowed us to explore the posterior probability distributions of the modeling parameters. Uniform priors were adopted for the kinetic temperature (T_{K}), H_2 number density (n_{H_2}), ^{13}CO column density [$\log(N_{^{13}\text{CO}})$], and the C^0 -to- ^{13}CO abundance ratio $N_{\text{C}^0}/N_{^{13}\text{CO}}$. These parameters were allowed to vary within the following ranges: $T_{\text{K}} = 5 - 300$ K, $n_{\text{H}_2} = 10^2 - 10^7 \text{ cm}^{-3}$, $N_{^{13}\text{CO}} = 10^{13} - 10^{19} \text{ cm}^{-2}$, and $N_{\text{C}^0}/N_{^{13}\text{CO}} = 0.1 - 100$.

The posterior distributions were computed as the product of the prior probability distributions and the likelihood function. We adopted a Gaussian likelihood of the form $\mathcal{L} \propto \exp(-\chi^2/2)$, where

$$\chi^2 = \sum_i \left(\frac{I_{\text{obs},i} - I_{\text{mod},i}}{\sigma_i} \right)^2, \quad (\text{S2})$$

with $I_{\text{obs},i}$, $I_{\text{mod},i}$, and σ_i representing the observed, modeled integrated intensities, and the corresponding 1σ observational uncertainties, respectively. For RCW 120, the fit included six transitions: $\text{CO} (1 - 0)$, $^{13}\text{CO} (1 - 0)$, $\text{CO} (3 - 2)$, $^{13}\text{CO} (3 - 2)$, $\text{CO} (4 - 3)$, and $[\text{CI}] (^3P_1 - ^3P_0)$. For RCW 79,

²<https://home.strw.leidenuniv.nl/~moldata/>

four lines were used: CO (1–0), ^{13}CO (1–0), CO (4–3), and [CI] ($^3P_1 - ^3P_0$). The MCMC chains were run with 10 walkers and 6000 steps following an initial burn-in phase, ensuring convergence of the sampling. The final parameter estimates and their 1σ uncertainties were derived from the 16th and 84th percentiles of the posterior distributions.

Figure S1 presents a representative example of the modeling results for RCW 120A, where all physical parameters are well constrained. In contrast, n_{H_2} is not well constrained for RCW 79A and RCW 79B due to the limited number of detected transitions. To improve the reliability of the results for these two sources, we restrict n_{H_2} to the range of $10^3 - 10^5 \text{ cm}^{-3}$ in the modeling. While n_{H_2} remains poorly constrained and carries larger uncertainties, the other parameters are robustly determined. A summary of the derived parameters for all four regions is presented in Table S2.

PDR Models

As demonstrated by previous studies, the intensity ratios between the transitions of C^+ , C^0 , and CO can be used to infer FUV radiation field strengths and gas densities (69, 70, 71). Here, we adopted both homogeneous and clumpy PDR models available through the PDR Toolbox³ (71). Following previous studies (71), we used the PDR Toolbox to fit selected observed line ratios that are effective tracers of local physical conditions.

Various geometries have been proposed to model PDR structures. In this study, we primarily adopted two suites of PDR models: the Wolfire–Kaufman model and the KOSMA- τ model (69, 70). The former assumes a plane-parallel geometry and corresponds to the “Wolfire–Kaufman 2020 (wk2020)” implementation, while the latter is based on an ensemble of spherical clumps, either with a mass spectrum (referred to as “clumpy”) or a single clump mass (“non-clumpy”), as implemented in the KOSMA- τ model. In all models, we assume typical solar metallicity ($z = 1$). In the KOSMA- τ models, the clump mass is another free parameter. We use $1 M_{\odot}$ as a fiducial case for the clump mass, and test the variation of the clump mass in the following calculations.

Using RCW 120A as a representative case, we examine the observed line ratios as a function of the local radiation field strength and gas density in Figure S2. These comparisons demonstrate that multi-line observations can effectively constrain both parameters. To refine the model constraints,

³<https://dustem.astro.umd.edu/>

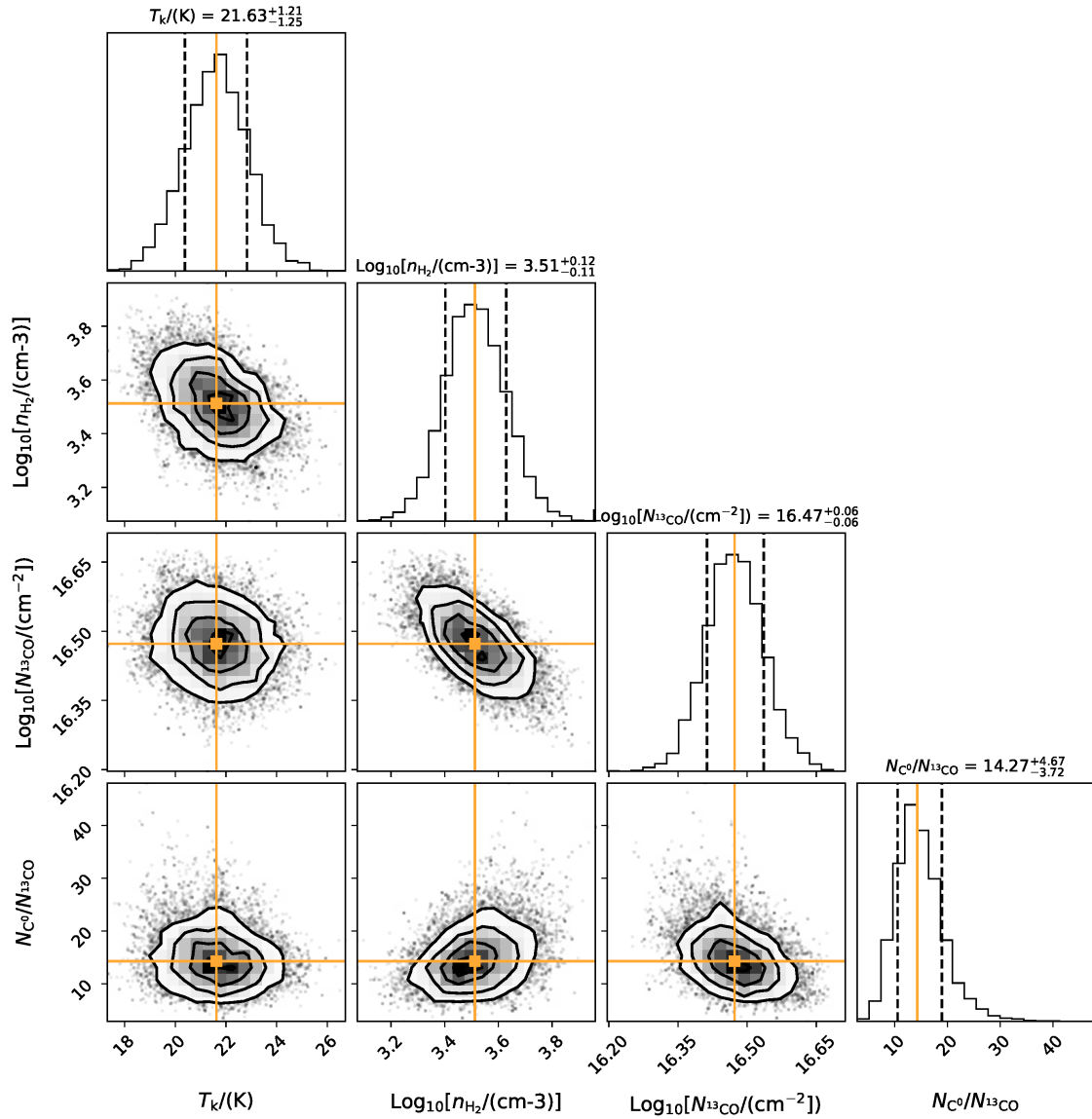


Figure S1: Posterior probability distributions of T_k , n_{H_2} , $\log(N_{\text{C}^0})$, and $N_{\text{C}^0}/N_{\text{C}^0}$ for RCW 120A from the RADEX models, with the maximum posterior possibility point in the parameter space highlighted by orange lines and points. Contours represent the 0.5, 1.0, 1.5, and 2.0 σ confidence intervals. The vertical dashed lines represent the 1 σ dispersion.

we incorporate archival low- J transitions of CO and ^{13}CO (see Section *Archival Data* in the supplementary materials). For the [CII] line, we considered only the narrow velocity component in the fitting, as the broad component is not detected in CO, ^{13}CO , or [CI] lines and likely originates from a physically distinct gas component. Although self-absorption is present in the [CII] spectra of RCW 120A and RCW 120B (see Figure 4), Gaussian fitting still provides a reasonable estimate of the total flux.

Figure S3 shows the modeling results of RCW 120A using the KOSMA- τ clumpy PDR framework, assuming a maximum clump mass of $1 M_{\odot}$. Parameter estimation is also performed with the MCMC method, similar to that described in Section *Non-LTE Analysis* of the supplementary materials. The same procedure is applied to other PDR models, and the derived radiation field strengths and gas densities across the selected regions are summarized in Table S2.

In the KOSMA- τ models, the clump mass might bias the inferred physical conditions. To assess this effect, we explore models with maximum clump masses of 0.1, 1, 10, and $100 M_{\odot}$. In the clumpy PDR model, the results remain largely insensitive to variations in clump mass, indicating robustness against this parameter. In contrast, the non-clumpy version of the KOSMA- τ model shows a strong dependence on clump mass. Increasing the clump mass systematically yields higher estimates for both gas density and incident radiation field strength.

We further compare the results of these PDR models with our non-LTE analysis (see Section *Non-LTE Analysis* in the supplementary materials). In the case of a plane-parallel PDR, reproducing the observed line intensities requires very high gas densities and FUV radiation fields. However, such high gas densities are inconsistent with those derived from the non-LTE analysis, indicating that the plane-parallel scenario does not provide a satisfactory explanation for the observations. In contrast, the clumpy PDR model can reproduce the observed line properties with significantly lower gas densities and FUV field strengths. Taking the uncertainties into account, these values are in good agreement with the non-LTE results (see Section *Non-LTE Analysis* in the supplementary materials). Our findings thus favor a clumpy PDR structure over a homogeneous plane-parallel configuration in explaining the observed spectral characteristics.

The relationships between line ratios and radiation field strengths are investigated in Figure S4. The results show that the radiation field strength exhibits a strong correlation with the [CII]/[CI] integrated intensity ratio, but appears largely insensitive to the [CI]/CO (4 – 3) integrated intensity

ratio. This highlights [CII] emission as an effective tracer of the radiation field strength. Notably, the C^0/CO abundance ratios appear to be comparable in RCW 79 and RCW 120 (see S2), despite a difference in radiation field strength of more than a factor of three between the two regions (see Table S2). Given that C^0 and CO can coexist across a broad range of visual extinctions in clumpy PDRs, both species can remain similarly abundant in well-mixed zones. Alternatively, the transition layers between CO and C^0 may be similar across different radiation fields, or their contributions to the observed C^0/CO abundance ratios may be negligible. Together, these effects might account for the similar C^0/CO abundance ratios observed across environments with different radiation field strengths.

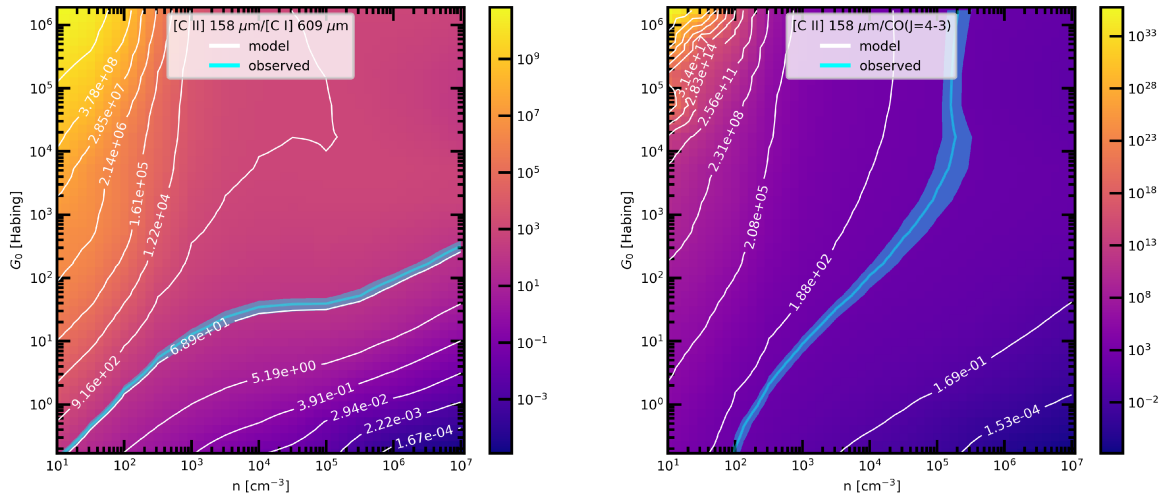


Figure S2: Predictions of the observed intensity ratios as a function of G_0 and n for RCW 120A, based on the clumpy PDR model. The solid lines represent the observed values, while the shaded regions indicate the 1σ errors.

Extinction Map

In addition to the visual extinction estimates presented in Section *Main text*, we also derive visual extinctions using Hi-GAL-based H_2 column density maps (see *Archival Data*). To match the angular resolution of our observations, the H_2 column density maps were convolved to a beam size of $6'$. Using the established relation between visual extinction and H_2 column density (45), we determine the extinction distributions for RCW 79 and RCW 120, as shown in Figure S5.

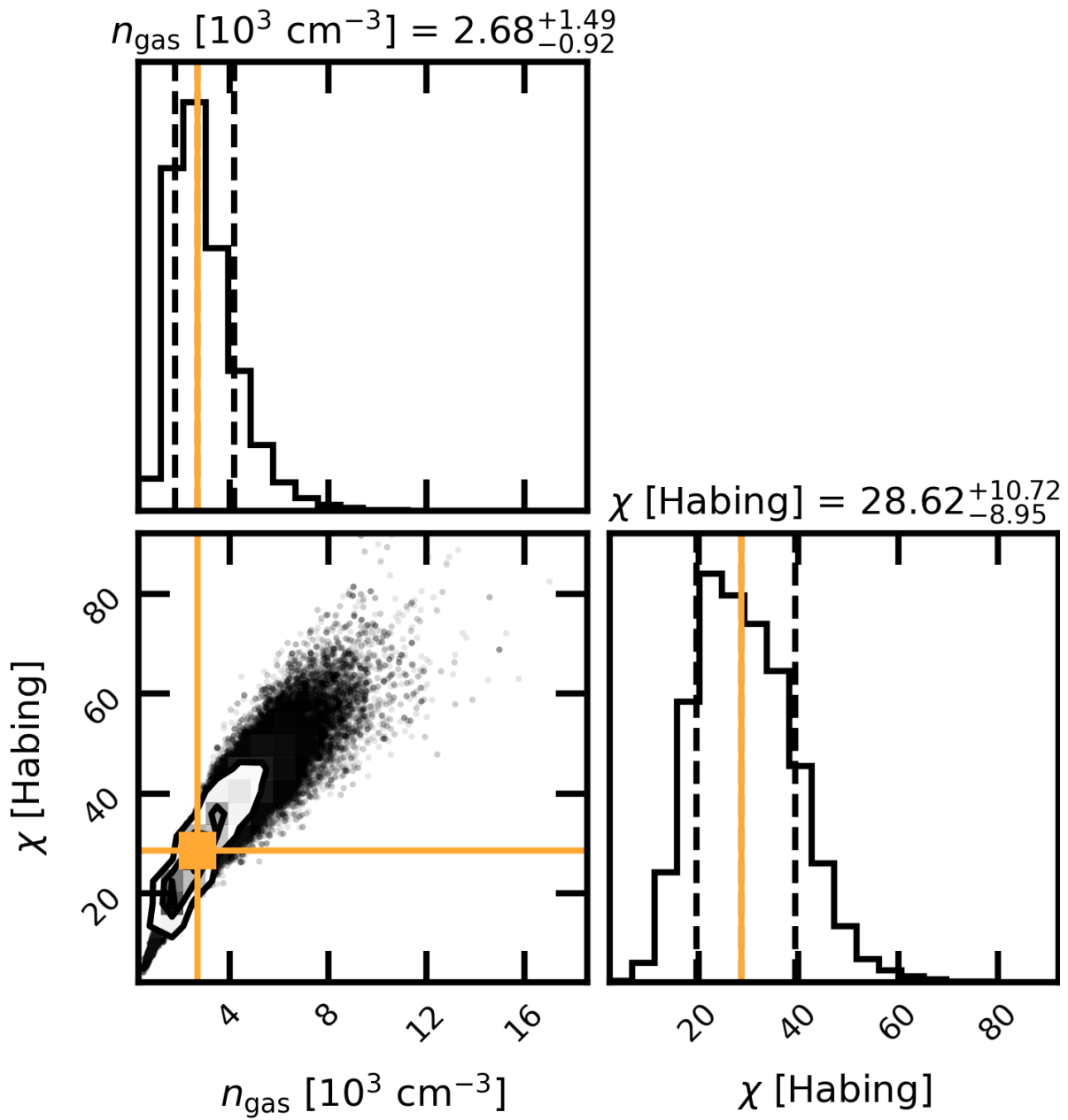


Figure S3: Posterior probability distributions of gas density and radiation field strength for RCW 120A from the KOSMA- τ clumpy PDR model, with the maximum posterior possibility point in the parameter space highlighted by orange lines and points. Contours represent the 0.5, 1.0, 1.5, and 2.0σ confidence intervals. The vertical dashed lines represent the 1σ dispersion.

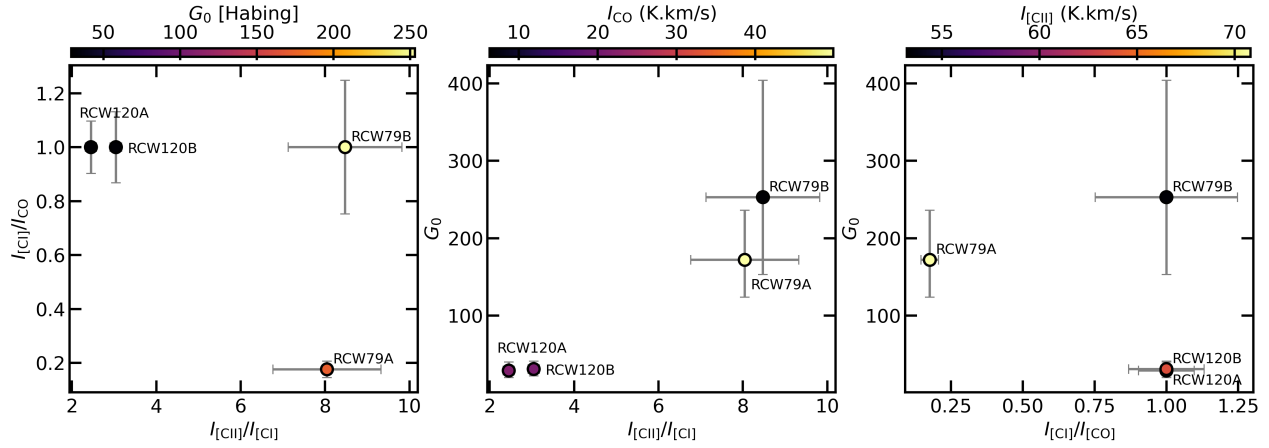


Figure S4: Relationship between line ratios and radiation field strength. *Left:* Observed integrated intensity ratio of [CI] to CO (4 – 3) as a function of the [CII]/[CI] ratio, with points colored by radiation field strength. *Middle:* [CI]/CO (4 – 3) ratio versus radiation field strength, colored by CO (4 – 3) integrated intensity. *Right:* Radiation field strength plotted against the [CI]/CO (4 – 3) ratio, with colors indicating [CII] integrated intensity.

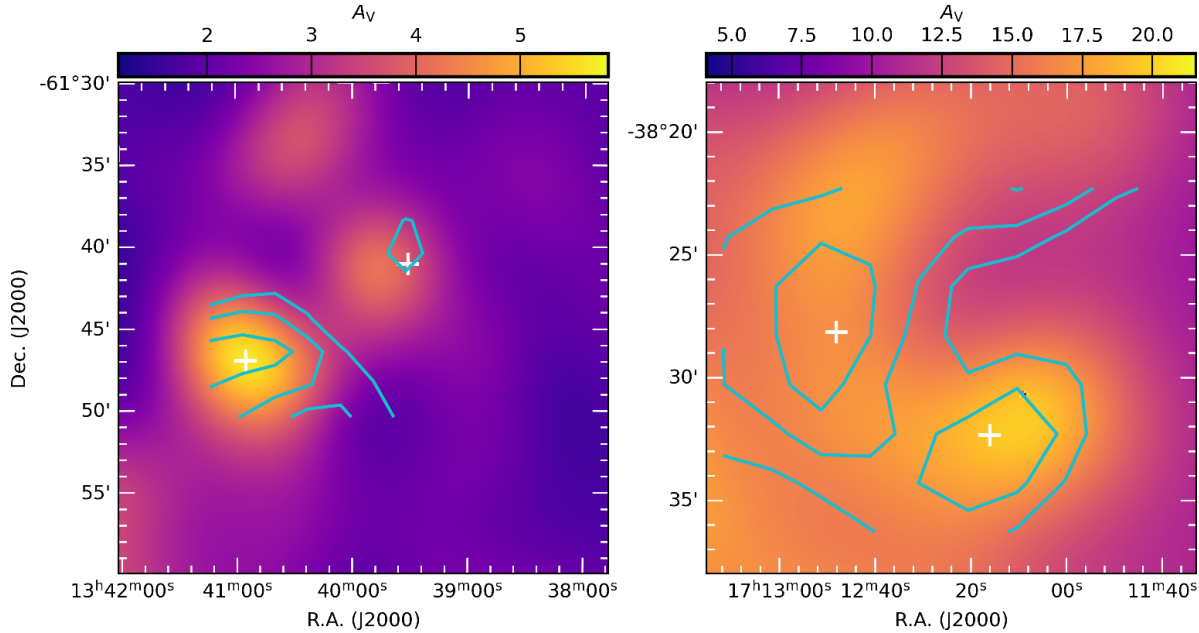


Figure S5: Extinction maps of RCW 79 and RCW 120. The overlaid [CI] integrated intensity contours are identical to those shown in Figure 2. The white pluses mark the positions of the four selected regions.

The visual extinctions are within the range of 1.5–5.7 and 4.9–21.5 for RCW 79 and RCW 120, respectively. This independent method yields visual extinctions of approximately 6, 4, 17, and 19 toward RCW 79A, RCW 79B, RCW 120A, and RCW 120B, respectively.

Flux Calibration

Absolute flux calibration was performed by comparing the integrated intensity of [CI] (${}^3P_1 - {}^3P_0$) from NGC 6334I obtained with ATE60 and APEX. The APEX data were observed under the large-scale [CI] mapping project of NGC 6334 (Project ID: M9516C_0109, PI: Sudeep Neupane). The APEX data were convolved to the ATE60’s angular resolution of 240'', and were calibrated with a main beam efficiency of 60%⁴. This comparison indicates a main beam efficiency of \sim 35% for ATE60 (see Figure S6), which was subsequently used to establish the main beam brightness temperature scale of all ATE60 data. The velocity was calibrated with respect to the local standard of rest (LSR), and the excellent agreement between the ATE60 and APEX data confirms the accuracy of the velocity calibration (see Figure S6). The absolute flux calibration uncertainties were assumed to be 20%.

Pointing

The pointing model was first established toward Canopus using an accompanying off-axis optical telescope. However, the accuracy is not high enough with respect to the ATE60’s HPBWs. Based on previous studies (72), the distributions of ${}^{13}\text{CO}$ (1 – 0) and CO (4 – 3) are similar on scales of \gtrsim 1 pc. To assess the residual pointing errors after the correction from the optical telescope, we compared Mopra ${}^{13}\text{CO}$ (1 – 0) data with our ATE60 CO (4 – 3) data. The ${}^{13}\text{CO}$ (1 – 0) data were convolved to have an angular resolution of 270'' for comparison. The comparison revealed an accuracy of \lesssim 3' in right ascension and declination (see Figure S7A). To further improve the pointing accuracy, we refined the pointing by cross-matching bright, compact sources in CO (4 – 3) with ${}^{13}\text{CO}$ (1 – 0), assuming a common spatial origin for these lines. The peak position in the CO (4 – 3) map was used to estimate the offset in azimuth and elevation, which was assumed to be identical across the entire map. Incorporating the offset, the observed coordinates were then re-calculated. The updated

⁴<https://www.apex-telescope.org/telescope/efficiency/?yearBy=2024>

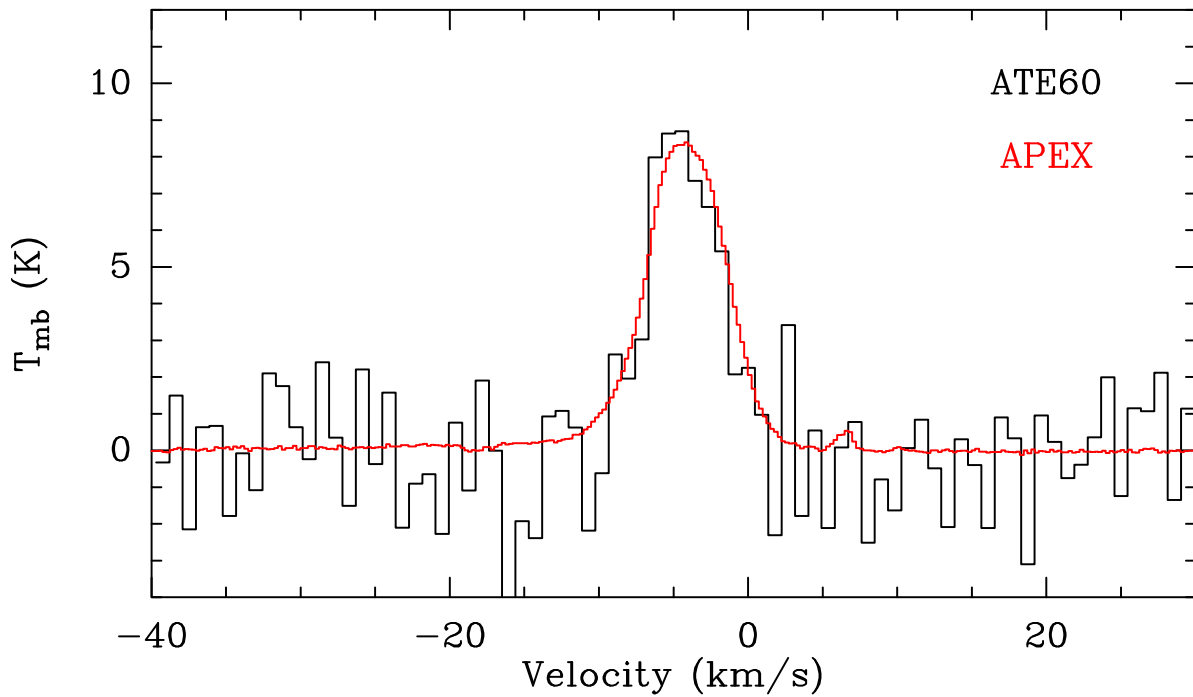


Figure S6: Comparison of [CI] ($^3P_1 - ^3P_0$) spectra of NGC 6334I obtained with ATE60 and APEX. Spectra from ATE60 and APEX are shown in black and red, respectively. Main beam efficiencies of 35% and 60% were assumed for the ATE60 and APEX data, respectively, yielding good consistency between the two datasets.

coordinates were no longer regularly spaced, prompting re-gridding of the data for subsequent analysis. As shown in Figure S7B, the regridded ATE60 CO (4 – 3) image exhibits a good spatial agreement with the Mopra ^{13}CO (1 – 0) image, demonstrating the effectiveness of our pointing correction method. Ultimately, the pointing error was estimated to be $\lesssim 1'$ after correction.

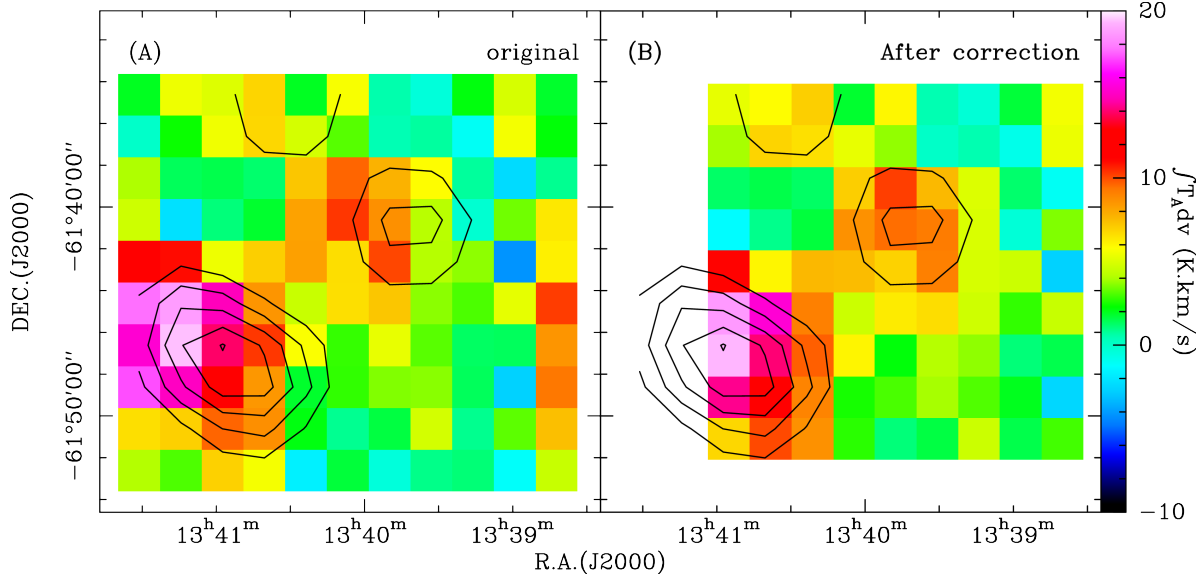


Figure S7: Distribution of CO (4 – 3) and ^{13}CO (1 – 0) in RCW 79. Integrated-intensity map of CO (4 – 3) overlaid with ^{13}CO (1 – 0) contours, before (panel A) and after (panel B) pointing correction. The Mopra ^{13}CO (1 – 0) data have been convolved to 270'', matching the beam size of our CO (4 – 3) data. The ^{13}CO (1 – 0) contours start at 8 K km s^{-1} and increase by 2 K km s^{-1} . Both maps are integrated over the velocity range of -40 to -30 km s^{-1} . In panel (b), the image has been cropped to exclude artifacts introduced by the re-gridding process.

Table S1: Observed properties of CO, [CI], and [CII] transitions toward the selected positions in RCW 79 and RCW 120 at a common angular resolution of 6'. Source: source name; α_{J2000} : right ascension; δ_{J2000} : declination; Transition: observed spectral transition; v_{lsr} : velocity centroid; Δv : FWHM line width; T_p : peak main beam temperature; $\int T_{\text{mb}} dv$: Integrated intensity.

Source	(α_{J2000}) ($^{\text{h:m:s}}$)	(δ_{J2000}) ($^{\circ}:\text{':}''$)	Transition	v_{lsr} (km s^{-1})	Δv (km s^{-1})	T_p (K)	$\int T_{\text{mb}} dv$ (K km s^{-1})
RCW 79A	13:40:55	-61:46:59	CO (1 - 0)	-46.7 \pm 0.1	4.8 \pm 0.1	6.8 \pm 0.3	35.0 \pm 0.6
			^{13}CO (1 - 0)	-46.7 \pm 0.1	3.6 \pm 0.1	3.1 \pm 0.1	11.9 \pm 0.2
			CO (4 - 3)	-46.5 \pm 0.2	5.6 \pm 0.5	8.4 \pm 0.3	49.9 \pm 3.4
			[CI] ($^3P_1 - ^3P_0$)	-46.2 \pm 0.3	4.1 \pm 0.7	2.0 \pm 0.3	8.8 \pm 1.4
			[CII] ($^2P_{3/2} - ^2P_{1/2}$) ^a	-47.5 \pm 0.1	18.2 \pm 0.2	2.3 \pm 0.2	44.3 \pm 0.5
				-46.4 \pm 0.1	4.8 \pm 0.1	5.2 \pm 0.2	26.5 \pm 0.2
RCW 79B	13:39:31	-61:41:04	CO (1 - 0)	-46.7 \pm 0.1	3.8 \pm 0.2	3.9 \pm 0.3	16.5 \pm 0.6
			^{13}CO (1 - 0)	-46.8 \pm 0.1	4.0 \pm 0.3	1.4 \pm 0.2	6.1 \pm 0.4
			CO (4 - 3)	-46.6 \pm 0.1	5.1 \pm 0.4	4.0 \pm 0.5	21.8 \pm 1.2
			[CI] ($^3P_1 - ^3P_0$)	-46.2 \pm 0.4	4.5 \pm 0.8	1.3 \pm 0.3	6.3 \pm 1.0
			[CII] ($^2P_{3/2} - ^2P_{1/2}$) ^a	-46.7 \pm 0.1	16.7 \pm 0.3	1.9 \pm 0.1	34.1 \pm 0.5
				-47.0 \pm 0.1	5.0 \pm 0.1	3.6 \pm 0.1	19.3 \pm 0.2
RCW 120A	17:12:48	-38:28:10	CO (1 - 0)	-8.4 \pm 0.1	6.5 \pm 0.1	11.7 \pm 0.8	80.8 \pm 0.7
			^{13}CO (1 - 0)	-7.8 \pm 0.1	4.2 \pm 0.1	5.8 \pm 0.8	26.0 \pm 0.4
			CO (3 - 2)	-7.8 \pm 0.1	6.3 \pm 0.1	9.4 \pm 0.3	62.8 \pm 0.3
			^{13}CO (3 - 2)	-7.3 \pm 0.1	3.3 \pm 0.1	4.3 \pm 0.1	14.8 \pm 0.1
			CO (4 - 3)	-7.6 \pm 0.1	5.1 \pm 0.2	8.8 \pm 0.6	47.9 \pm 1.8
			[CI] ($^3P_1 - ^3P_0$)	-7.5 \pm 0.1	4.8 \pm 0.3	4.3 \pm 0.5	21.7 \pm 1.1
			[CII] ($^2P_{3/2} - ^2P_{1/2}$) ^a	-8.5 \pm 0.2	17.5 \pm 0.6	1.1 \pm 0.2	20.9 \pm 0.8
				-6.8 \pm 0.1	6.0 \pm 0.1	5.0 \pm 0.3	32.3 \pm 0.2
RCW 120B	17:12:16	-38:32:22	CO (1 - 0)	-8.3 \pm 0.1	6.4 \pm 0.1	10.7 \pm 0.7	72.3 \pm 0.4
			^{13}CO (1 - 0)	-7.9 \pm 0.1	4.0 \pm 0.1	5.2 \pm 0.3	22.5 \pm 0.3
			CO (3 - 2)	-7.8 \pm 0.1	6.7 \pm 0.5	8.4 \pm 0.5	59.3 \pm 0.2
			^{13}CO (3 - 2)	-7.3 \pm 0.1	3.3 \pm 0.1	4.3 \pm 0.1	14.9 \pm 0.1
			CO (4 - 3)	-7.7 \pm 0.1	5.8 \pm 0.3	9.5 \pm 0.7	58.6 \pm 2.6
			[CI] ($^3P_1 - ^3P_0$)	-7.9 \pm 0.1	5.2 \pm 0.3	3.7 \pm 0.3	20.3 \pm 0.9
			[CII] ($^2P_{3/2} - ^2P_{1/2}$) ^a	-9.7 \pm 0.1	13.6 \pm 0.3	2.6 \pm 0.2	37.1 \pm 0.8
				-6.9 \pm 0.1	5.2 \pm 0.1	4.8 \pm 0.4	26.5 \pm 0.2

^a [CII] spectra were fitted by assuming two velocity components, consisting of a broad-line-width and a narrow-line-width component.

Table S2: Physical properties of the selected positions derived from the carbon's three primary phases. T_K : gas kinetic temperature; n_{H_2} : H₂ number density; $N_{^{13}\text{CO}}$: ¹³CO column density; N_{C^0} : C⁰ column density; $N_{C^0}/N_{^{13}\text{CO}}$: the column density ratio between C⁰ and ¹³CO; N_{C^0}/N_{CO} : the column density ratio between C⁰ and CO; n_{gas} : gas density; G_0 radiation field;

Source	Non-LTE					
	T_K (K)	$\log_{10}(n_{H_2})$ (cm ⁻³)	$\log_{10}(N_{^{13}\text{CO}})$ (cm ⁻²)	N_{C^0} ($\times 10^{17}$ cm ⁻²)	$N_{C^0}/N_{^{13}\text{CO}}$	N_{C^0}/N_{CO}^a
RCW 79A	$14.8^{+1.2}_{-1.2}$	$4.3^{+0.5}_{-0.6}$	$16.2^{+0.1}_{-0.1}$	$2.4^{+1.3}_{-1.0}$	$15.2^{+7.5}_{-5.3}$	$0.30^{+0.15}_{-0.11}$
RCW 79B ^b	$15.4^{+1.2}_{-1.2}$	$4.3^{+0.5}_{-0.6}$	$15.9^{+0.1}_{-0.1}$	$2.1^{+1.2}_{-0.9}$	$25.8^{+14.3}_{-9.9}$	$0.52^{+0.29}_{-0.20}$
RCW 120A	$21.5^{+1.3}_{-1.3}$	$3.5^{+0.1}_{-0.1}$	$16.5^{+0.1}_{-0.1}$	$4.6^{+2.0}_{-1.6}$	$14.4^{+5.2}_{-3.9}$	$0.29^{+0.10}_{-0.08}$
RCW 120B	$16.6^{+1.1}_{-1.1}$	$3.8^{+0.1}_{-0.1}$	$16.4^{+0.1}_{-0.1}$	$5.7^{+2.8}_{-2.2}$	$22.5^{+10.0}_{-7.3}$	$0.45^{+0.20}_{-0.15}$

Source	PDR					
	plane-parallel(wk2020)		non-clumpy(kt2020@1 M_{\odot})		clumpy(kt2020@1 M_{\odot})	
	n_{gas} (cm ⁻³)	G_0 (Habing)	n_{gas} (cm ⁻³)	G_0 (Habing)	n_{gas} (cm ⁻³)	G_0 (Habing)
RCW 79A	$1.1^{+0.5}_{-0.3} \times 10^5$	751^{+268}_{-200}	$3.1^{+2.0}_{-1.1} \times 10^3$	102^{+34}_{-30}	$1.8^{+1.1}_{-0.7} \times 10^4$	172^{+64}_{-48}
RCW 79B ^b	$7.6^{+4.9}_{-2.6} \times 10^4$	1957^{+982}_{-669}	$8.3^{+6.6}_{-3.1} \times 10^3$	86^{+53}_{-34}	$6.4^{+4.0}_{-2.4} \times 10^3$	253^{+151}_{-100}
RCW 120A	$2.0^{+0.2}_{-0.2} \times 10^4$	69^{+13}_{-11}	$4.9^{+2.3}_{-1.8} \times 10^3$	17^{+7}_{-5}	$2.7^{+1.5}_{-0.9} \times 10^3$	29^{+11}_{-9}
RCW 120B	$2.4^{+0.2}_{-0.2} \times 10^4$	74^{+14}_{-12}	$6.7^{+3.3}_{-2.2} \times 10^3$	18^{+7}_{-5}	$3.7^{+2.1}_{-1.4} \times 10^3$	31^{+10}_{-9}

^a The N_{C^0}/N_{CO} ratio was derived by scaling the measured $N_{C^0}/N_{^{13}\text{CO}}$ ratio by the adopted ¹²C/¹³C isotopic ratio of 50.

^b The large uncertainties of RCW 79B are mainly caused by the low signal-to-noise ratios of [CI] data. The H₂ number density is not well constrained in the RADEX model.